

PDF bias and flavor dependence in TMD distributions

Marcin Bury^a Francesco Hautmann^{b,b'} Sergio Leal-Gomez^c Ignazio Scimemi^d Alexey Vladimirov^e Pia Zurita^e

^a*Jerzy Haber Institute of Catalysis and Surface Chemistry, Polish Academy of Sciences, Niezapominajek 8, 30-239 Kraków, Poland*

^b*Elementaire Deeltjes Fysica, Universiteit Antwerpen, B 2020 Antwerpen*

^{b'}*Theoretical Physics Department, University of Oxford, Oxford OX1 3PU*

^c*Wien Universität, Faculty of Physics, Boltzmannngasse 5, A-1090 Vienna, Austria*

^d*Dpto. de Física Teórica & IPARCOS, Universidad Complutense de Madrid, E-28040 Madrid, Spain*

^e*Institut für Theoretische Physik, Universität Regensburg, D-93040 Regensburg, Germany*

E-mail: marcin.bury@ifj.edu.pl, francesco.hautmann@physics.ox.ac.uk,
sergio.leal.gomez@univie.ac.at, ignazios@ucm.es, alexey.vladimirov@ur.de,
maria.zurita@ur.de

ABSTRACT: Transverse momentum dependent (TMD) distributions match collinear parton density functions (PDF) in the limit of small transverse distances, which is accounted for by global extractions of TMD distributions. We study the influence of the PDF choice on the determination of unpolarized TMDPDFs and the description of TMD Drell-Yan-pair and Z-boson production data. We find that PDF essentially biases the extraction of TMDPDF. The bias is alleviated once the PDF uncertainty is taken into account and the non-perturbative TMD profile is flavor-dependent. Both points improve the agreement between theory and experiment, substantially increase the uncertainty in extracted TMD distributions, and should be taken into account in future global analyses.

Contents

1	Introduction	1
2	Evidences of PDF bias	2
3	Theory inputs	4
3.1	DY factorization formula	5
3.2	Non-perturbative models	6
4	TMD data sets	8
4.1	Complete data set	8
4.2	Reduced data set	9
5	Statistical framework	10
5.1	Definition of the χ^2 -function	10
5.2	Input PDFs and their uncertainties	11
5.3	Determination of uncertainties & presentation of the result	12
6	Results & discussion	13
6.1	Agreement between data and theory	13
6.2	Extracted TMD distributions	15
6.3	Predictions for W -boson production	19
7	Conclusions	21

1 Introduction

While determinations of the proton’s collinear parton distribution functions (PDFs) [1] from fits to experimental data have been carried out for four decades, and PDFs are nowadays known with high precision, the systematic investigation of the transverse momentum dependent (TMD) [2] distribution functions has started much more recently. In the last few years determinations of TMD distributions from fits to experimental data have been performed in the context of low transverse momentum Drell-Yan (DY) production and semi-inclusive deep inelastic scattering (SIDIS) [3–8], small- x deep inelastic scattering [9], nonlinear TMD evolution [10], parton branching [11]. The results are collected in the public library TMDlib [12, 13], similarly to the case of PDF.

A physical cross section σ with hard scale Q and measured transverse momentum $q_T \ll Q$ is described in terms of TMD distributions by a factorization formula with the schematic form, up to power corrections in q_T/Q and Λ/Q ,

$$\frac{d\sigma}{dq_T^2} = \sum_{i,j} \int d^2b \, e^{ib \cdot q_T} \sigma_{ij}^{(0)} f_{1,i \leftarrow h1}(x_1, b; \mu, \zeta_1) f_{1,j \leftarrow h2}(x_2, b; \mu, \zeta_2), \quad (1.1)$$

where b is the transverse distance Fourier conjugate to transverse momentum, $\sigma_{ij}^{(0)}$ are perturbatively calculable partonic cross sections, and f_i and f_j are TMD parton distributions, which depend on the mass and rapidity scales μ and ζ through appropriate evolution equations, involving both perturbative and non-perturbative (NP) components, and are to be determined from fits to experiment. Current fits to TMD distributions are performed by using, besides the TMD factorization and evolution framework, additional inputs which exploit the relationship between TMD distributions and the collinear PDFs. These relations follow from the operator product expansion (OPE) applied to the TMD operator.

The OPE expresses the TMD distributions in terms of PDFs via perturbatively calculable coefficients, as follows

$$f_{1,f\leftarrow h}(x, b; \mu, \zeta) = \sum_{f'} \int_x^1 \frac{dy}{y} C_{f\leftarrow f'}(y, b; \mu, \zeta) q_{f'}\left(\frac{x}{y}, \mu\right) + O(b^2), \quad (1.2)$$

where $f_i(x, b; \mu, \zeta)$ is the TMD distribution, $q_j(x, \mu)$ is the PDF, C_{ij} are the Wilson coefficient function, μ and ζ are factorization scales, the subscripts f and f' indicate parton flavors, and the last term on the right hand side denotes a power suppressed correction at small b . Eqn. (1.2) is used in the context of precision studies of the DY transverse momentum q_T spectrum at the Large Hadron Collider (LHC) [14]. It is instrumental in performing comparisons, at the level of small- q_T logarithmic resummations, between computer codes `artemide` [5] and `NangaParbat` [6], based on TMD distributions, and computer codes `DYturbo` [15], `reSolve` [16], `Radish` [17], `SCETlib` [18], and `CuTe` [19], which perform perturbative small- q_T resummation without systematically introducing TMD distributions.

The use of the OPE grants certain advantages in the TMD phenomenology but introduces specific issues that we address in this work. On one hand, OPE relations usefully supplement the TMD factorization by increasing the predictive power of TMD phenomenology. On the other hand, it binds a TMD distribution to the collinear PDF and significantly reduces the freedom to determine TMD distributions independently and in agreement with the data, making TMD analysis vulnerable to the tensions and methodology of collinear phenomenology. We refer to this as a *PDF bias*.

The PDF bias problem runs deeper than one may guess at the first glance, and evidences of this are clearly visible in the earlier studies. We summarize such evidences using the example of the fit made in ref. [3] in sec. 2. As we shall see, although collinear PDFs are nowadays known with exceeding precision, the differences among PDF sets and their uncertainties (see Fig. 1) turn out to play a very significant role in TMD phenomenology. A natural resolution of PDF bias could be achieved through a full joint PDF and TMD fit of experimental data. However, this is an extremely challenging task with the currently available tools. We quantify these effects in the concrete setting of a TMD global fit for the first time. To carry out this investigation, we consider unpolarized DY process at small q_T . We use the implementation of the TMD factorization theorem as in refs. [3, 4], and perform fits of experimental measurements using different PDF sets, accounting (for the first time) for PDF uncertainties. We demonstrate that the PDF bias problem is closely related to the flavor dependence of TMDPDF, and partially resolved by accounting for flavor dependence in the fitting ansatz. This work can be classified as an exploratory study, with the goal of obtaining a fit of TMD distributions from DY and Z-boson production data such that it a) accounts for the PDF uncertainty, b) gives a consistent statistical picture, and c) is valid for collinear PDFs extracted by different groups. We select HERA20 [20], MSHT20 [21], CT18 [22] and NNPDF3.1 [23] as representatives of different methodological approaches at NNLO.

The article is structured as follows. We start in sec. 2 with the characterization of the PDF bias effects and their impact in the description of the DY spectrum. Sec. 3 provides basic theoretical inputs and notation. Sec. 4 presents the data used in the analysis. The statistical methods are reported in sec. 5. Sec. 6 presents the results and the discussion of their consequences. We give conclusions in sec. 7.

2 Evidences of PDF bias

In this section we present observations that illustrate the problem of PDF bias. Separately, each of the discussed issues is minor, however they are not independent but present evidences of the global problem of PDF bias.

As an example, we use the fit of unpolarized TMD distributions made in ref. [3], hereafter referred to as SV19. The TMD distributions are defined according to the ansatz

$$f_{1,f\leftarrow h}(x, b; \mu, \zeta) = \sum_{f'} \int_x^1 \frac{dy}{y} C_{f\leftarrow f'}(y, b; \mu, \zeta) q_{f'}\left(\frac{x}{y}, \mu\right) f_{\text{NP}}^f(x, b). \quad (2.1)$$

Here f_{NP} is a function which contains power corrections to eqn. (1.2), behaves as $f_{\text{NP}}^f(x, b) \sim 1 + O(b^2)$ for $b \rightarrow 0$ and is to be fitted to experimental data. This ansatz exactly reproduces eqn.(1.2) for $b \rightarrow 0$

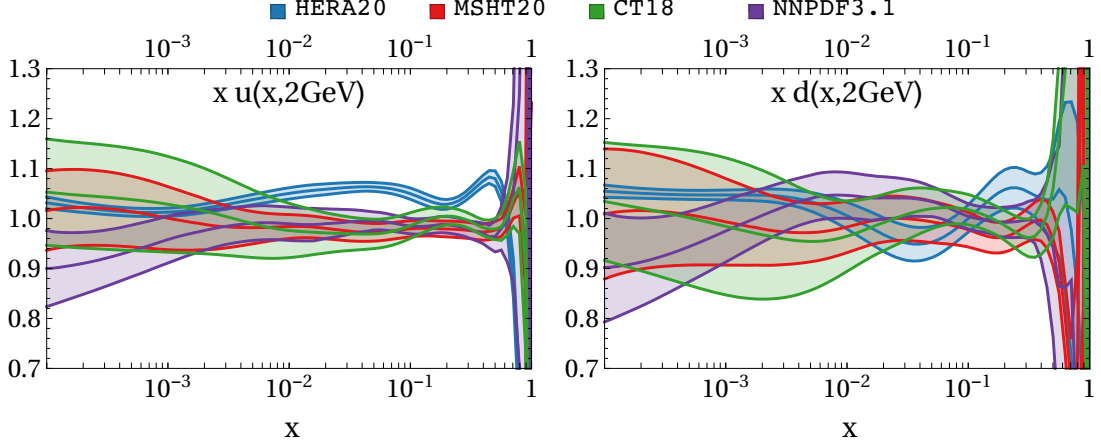


Figure 1: Comparison of the uncertainty bands of PDFs extracted by different groups for u and d quarks. The PDFs are weighted by an average of the central values.

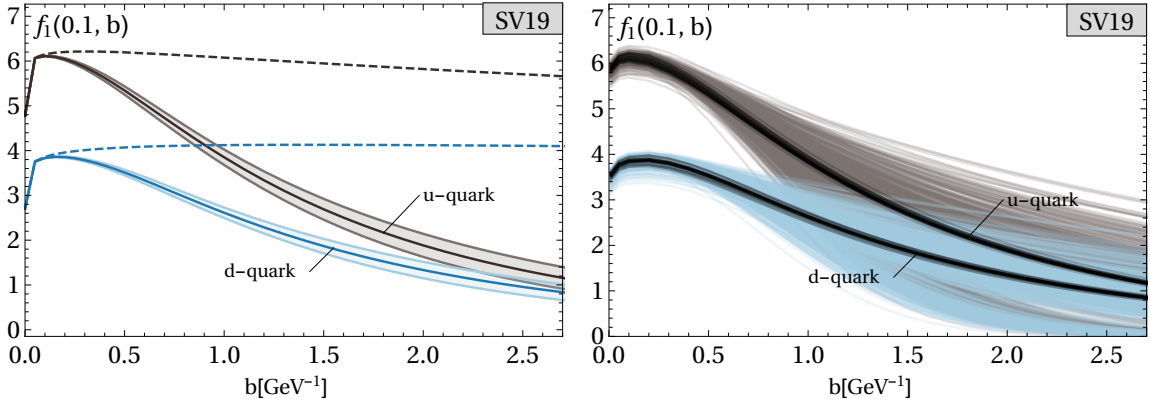


Figure 2: TMDPDFs from the SV19 fit [3]. Left: Comparison of u - and d -quark TMDPDFs as function of b (at $x = 0.1$). The dashed lines correspond to the TMDPDFs at $f_{\text{NP}} = 1$. Right: The SV19 extraction evaluated at different replicas of NNPDF3.1 collinear PDF. Black lines using the SV19 values for f_{NP} , lighter lines with fit of f_{NP} for each replica.

but allows for modifications at finite b . Such an ansatz is used in many fits, see e.g.[3–7, 24–26]. We are interested to examine effects of different collinear PDF sets and their uncertainties on the TMD extraction.

The left panel of fig. 2 shows the SV19 fit result [3] for the b dependence of the u -quark and d -quark TMD distributions at fixed x . The uncertainty band vanishes for $b \rightarrow 0$, where the value of TMD distribution is fixed by eqn. (1.2). However, we observe that the uncertainty band remains small also for larger values of b . E.g. at $b = 1 \text{ GeV}^{-1}$ it is only 2.2%, and at $b = 2 \text{ GeV}^{-1}$ it is 6.8%. Such a behavior is not specific to SV19 but was also observed in the fit of ref. [6], and indicates a significant model bias, which apparently can be removed by resolving the band at $b \rightarrow 0$. I.e. by inclusion of the uncertainty of the PDF extraction.

Given a fixed set of PDFs, we evaluate the error coming from the PDF uncertainty. This is shown in black in the right panel of fig. 2. The plot is done computing the TMDPDF according to eqn. (2.1) for each replica of the NNPDF3.1 PDF set (1000 replicas) [23] keeping f_{NP} fixed. This uncertainty band has an almost constant width starting at $b = 0$. The resulting uncertainty band in the cross-section is an order of magnitude larger than the original SV19: see left panel of fig. 3, where we show examples of Z-boson production in ATLAS and LHCb kinematics, calculated using the central PDF value. It happens because the integral for cross-section (1.1) at high-energy is dominated by the contribution at $b \sim 0$, and thus errors of PDF propagate to the observable almost directly.

So far, we have treated f_{NP} and q_f independently. Notwithstanding, both functions compose a single

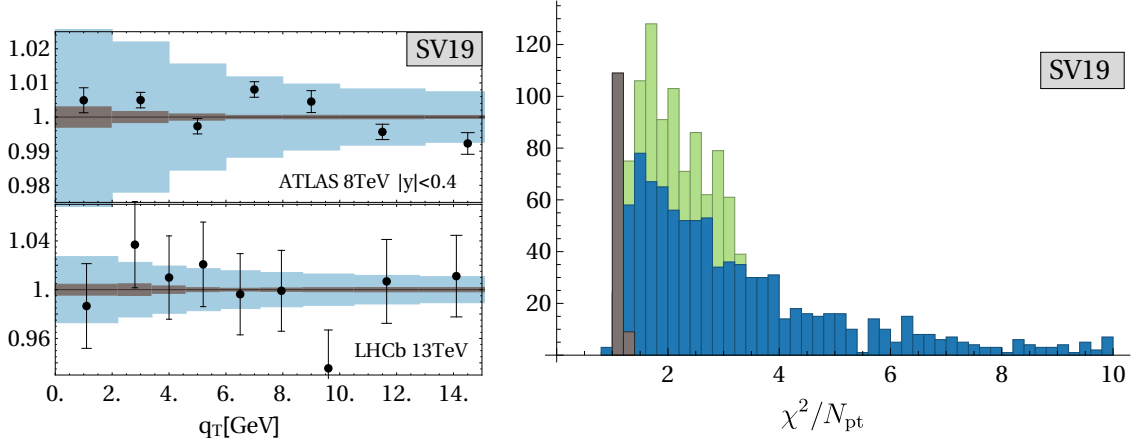


Figure 3: Left: Comparison of the uncertainty bands in Z-boson production cross-sections due to SV19 (dark gray) and NNPDF (blue). For better visual compression all data points are shifted by a common factor (1% for ATLAS, and 5% for LHCb). Right: Distribution of χ^2/N_{pt} for 100 replicas of SV19 (dark gray), and for 1000 replicas of NNPDF with f_{NP} from SV19 without fit (blue) and with fit (green).

TMDPDF. To reveal the correlation, we fit f_{NP} for each PDF replica and show the result in fig. 2. Clearly, the inclusion of the PDF uncertainty produces a broader, more realistic band for the TMDPDF, indicating that the PDF bias problem is alleviated.

However, the inclusion of the PDF uncertainty in the data description leads to another potential issue. We note that, while formally a specific PDF replica is just a part of the TMD modeling, most of the PDF replicas (more than 75%) have $\chi^2/N_{\text{pt}} > 2$, while the central replica describes the data with $\chi^2/N_{\text{pt}} \sim 1.1$. This behavior does not substantially change if f_{NP} is fitted for each PDF replica. The distribution of χ^2 -values over PDF replicas (right panel of fig. 3) shows an unsatisfactorily broad shape, with about 64% of the replicas having $\chi^2/N_{\text{pt}} > 2$. We have checked, that the unsatisfactory χ^2 -values for the subset of replicas are not due to a single problematic measurement but rather they are common to all data, indicating that such replicas have an inadequate shape and cannot fit TMD data.

Next, we examine the behavior of different PDF sets. We find that the issues described above are not specific to the NNPDF3.1 PDF set [23]. We perform similar tests using HERA20 [20] ($\chi_0^2/N_{\text{pt}} = 0.97$), MMHT14 [27] ($\chi_0^2/N_{\text{pt}} = 1.34$), CT14 [28] ($\chi_0^2/N_{\text{pt}} = 1.59$), PDF4LHC15 [29] ($\chi_0^2/N_{\text{pt}} = 1.53$), MSHT20 [21] ($\chi_0^2/N_{\text{pt}} = 1.25$), CT18 [22] ($\chi_0^2/N_{\text{pt}} = 1.26$), and CJ15n1o [30] ($\chi_0^2/N_{\text{pt}} = 1.82$). Here χ_0^2 is the χ^2 -value for the central PDF replica. All these PDF sets are characterized by the same issues as NNPDF3.1.

A key finding in this study concerns the functional parameterization of f_{NP} and its flavor dependence. We find that the SV19 profile function [3] is inadequate to address the PDF bias issue. In particular, the SV19 profile function is flavor independent and incorporates five free parameters, which control the behavior for $\sim b^2$, $\sim b^4$, and $b \rightarrow \infty$. However, this parametric freedom is not fully used in the SV19 fit, and there are some internal tensions that *i*) restrict the large- b profile to a relatively narrow region, and *ii*) make the result too sensitive to the collinear PDF input. We checked that incorporating more parameters into a flavor-independent f_{NP} does not solve these tensions. Instead, the solution is to be found in the flavor dependence of f_{NP} . We stress that the non-perturbative TMD behavior is flavor-dependent, and this dependence may not be reproduced solely by the PDF. Previous global TMD fits have ignored this effect. Once flavor dependence is added, the tensions among different PDF sets and within a single PDF set almost disappear, and the ordinary picture of statistical distributions is revealed. This leads to a more realistic uncertainty band for the unpolarized TMDPDF and predicted cross-sections.

3 Theory inputs

The TMD factorization theorem for the DY cross section has been derived in [31–34]. In this section, we summarize some basic notation and formulas that have been described with more details in ref. [3] and

used also in refs. [4, 5, 24, 25, 35–37]. The main feature of our realisation of TMD factorization is the ζ -prescription for TMD evolution, which is described in refs. [3, 38].

3.1 DY factorization formula

The TMD factorized expression for the cross-section of DY process $h_1 + h_2 \rightarrow \gamma^*/Z(\rightarrow \ell^+\ell^-) + X$ is valid in the regime

$$\mathbf{q}_T^2 \ll Q^2, \quad \text{and} \quad \Lambda^2 \ll Q^2, \quad (3.1)$$

where Q^2 is the invariant mass of the vector boson, \mathbf{q}_T is the transverse component of its momentum (relative to the scattering plane), and $\Lambda \sim 1\text{GeV}$ some generic hadron scale. In this regime, the differential cross-section can be written as

$$\begin{aligned} \frac{d\sigma}{dQ^2 dy d\mathbf{q}_T^2} = & \frac{2\pi}{3N_c} \frac{\alpha_{\text{em}}^2}{sQ^2} \sum_f \left[\mathcal{P}_1 \left(1 + \frac{\mathbf{q}_T^2}{2Q^2} \right) W_{f_1 f_1}^f(Q, \sqrt{\mathbf{q}_T^2}, x_1, x_2) + \dots \right] \\ & \times \left[z_l^{\gamma\gamma} z_f^{\gamma\gamma} + z_l^{\gamma Z} z_f^{\gamma Z} \frac{2Q^2(Q^2 - M_Z^2)}{(Q^2 - M_Z^2)^2 + \Gamma_Z^2 M_Z^2} + z_l^{ZZ} z_f^{ZZ} \frac{Q^4}{(Q^2 - M_Z^2)^2 + \Gamma_Z^2 M_Z^2} \right], \end{aligned} \quad (3.2)$$

where α_{em} is the fine-structure constant, y is the rapidity of the vector boson, M_Z and Γ_Z are the mass and width of the Z-boson, and the dots denote terms suppressed by \mathbf{q}_T^2/Q^2 . The index f runs over all active quark flavors. The factors z_i^{ab} are the combinations of vector and axial couplings for quarks and leptons:

$$z_f^{\gamma\gamma} = e_f^2, \quad (3.3)$$

$$z_f^{\gamma Z} = \frac{T_3 - 2e_f s_W^2}{2s_W^2 c_W^2}, \quad (3.4)$$

$$z_f^{ZZ} = \frac{(1 - 2|e_f|s_W^2)^2 + 4e_f^2 s_W^4}{8s_W^2 c_W^2}, \quad (3.5)$$

with e_f the charge of particle, s_W and c_W the sine and cosine of Weinberg angle, and T_3 the third component of the iso-spin. The factor $(1 + \mathbf{q}_T^2/(2Q^2))\mathcal{P}_1$ is the result of the convolution of the leading power hadron tensor with the lepton tensor. Here \mathcal{P}_1 is a projector which accounts for fiducial cuts [3, 5] ($\mathcal{P}_1 = 1$ if fiducial cuts are not implemented). The factor $W_{f_1 f_1}$ contains the information about the non-perturbative content

$$W_{f_1 f_1}^f(Q, q_T, x_1, x_2) = |C_V(-Q^2, \mu^2)|^2 \int_0^\infty db b J_0(bq_T) f_{1,f \leftarrow h_1}(x_1, b; \mu, \zeta_1) f_{1,\bar{f} \leftarrow h_2}(x_2, b; \mu, \zeta_2). \quad (3.6)$$

Here, f_1 is the unpolarized TMDPDF, C_V is the vector form factor of the quark, and J_0 is the Bessel function. The variables x_1 and x_2 are

$$x_1 = \sqrt{\frac{Q^2 + \mathbf{q}_T^2}{s}} e^{+y}, \quad x_2 = \sqrt{\frac{Q^2 + \mathbf{q}_T^2}{s}} e^{-y}. \quad (3.7)$$

The scaling variables μ and $\zeta_{1,2}$ are fixed as

$$\mu = Qc_2, \quad \zeta_1 = \zeta_2 = Q^2, \quad (3.8)$$

such that the logarithmic contribution to C_V is zero at $c_2 = 1$. The evolution of TMD distributions is given by the pair of equations [32, 34, 39]

$$\begin{aligned} \mu^2 \frac{\partial f_{1,f \leftarrow h}(x, b; \mu, \zeta)}{\partial \mu^2} &= \left(\Gamma_{\text{cusp}} \ln \frac{\mu^2}{\zeta} - \gamma_V(\mu) \right) f_{1,f \leftarrow h}(x, b; \mu, \zeta), \\ \zeta \frac{\partial f_{1,f \leftarrow h}(x, b; \mu, \zeta)}{\partial \zeta} &= -\mathcal{D}(b, \mu) f_{1,f \leftarrow h}(x, b; \mu, \zeta), \end{aligned} \quad (3.9)$$

where Γ_{cusp} is the anomalous dimension for the cusp of light-like Wilson lines, γ_V is the anomalous dimension of the quark vector form factor and \mathcal{D} is the NP Collins-Soper (CS) kernel. The solution of these equations

in our case is provided fixing scales according to the ζ -prescription [5, 38]. As a result, the evolved TMD distribution is

$$f_1(x, b; Q, Q^2) = \left(\frac{Q^2}{\zeta_Q(b, \mathcal{D})} \right)^{-\mathcal{D}(b, Q)} f_1(x, b), \quad (3.10)$$

where $\zeta_Q(b, \mathcal{D})$ is a function defined such that the reference TMD distribution is scale-independent [3, 24]. The reference TMD distribution on the r.h.s. of eqn. (3.10) is called *optimal* TMD distribution and is scaleless. In the ζ -prescription the optimal TMD distribution is disconnected from the CS kernel. Correlations between TMD distribution and CS kernel are studied in [36]. Another important feature is that $\zeta_Q(b, \mathcal{D})$ is known as a functional of \mathcal{D} and a particular implementation of CS kernel.

The perturbative orders used for each element of the cross section are summarized in the following table.

The definition of $\mathcal{D}_{\text{resum}}$ is given in the next section. The resulting cross section corresponds to NNLL'

H	$C_{f \leftarrow f'}$	Γ_{cusp}	γ_V	$\mathcal{D}_{\text{resum}}$	a_s running & PDF evolution
a_s^2	a_s^2	a_s^3	a_s^2	a_s^2	NNLO

according to the terminology in [14]. The selection of this setup is motivated by its numeric simplicity (in comparison to others with higher perturbative orders already calculated), and by the fact that PDF evolution and extraction is available only up to NNLO so that the implementation of higher orders does not significantly affect the extraction of NP TMD [3].

Let us note that our implementation of the TMD factorization contains terms of order $\sim \mathbf{q}_T^2/Q^2$, which in other implementations are considered as power corrections cf. e.g. [4, 6, 18, 31, 40]. Here we refer to power corrections only in relation to the hadronic tensor. In other words we always consider exactly the lepton tensor, the phase space volume, and parameters such as $x_{1,2}$ because they are universal, in the sense that they are independent of any expansion of the hadronic tensor. The terms of order $\sim \mathbf{q}_T^2/Q^2$ in eqn. (3.2) result from the convolution of the leptonic tensor with the leading-power hadronic tensor. These are numerically negligible in the regime of TMD factorization, and produce some small correction at higher values of q_T^2 (see dedicated study in ref. [3]). For a discussion about the power expansion of the hadronic tensor, see [41].

3.2 Non-perturbative models

The non-perturbative content of the DY differential cross section is enclosed in two independent functions: the CS kernel and the (optimal) TMD distribution. For the CS kernel we employ here the same model used in SV19. It reads

$$\mathcal{D}(b, \mu) = \mathcal{D}_{\text{resum}}(b^*(b), \mu) + c_0 b b^*(b), \quad (3.11)$$

where

$$b^*(b) = b \left(\sqrt{1 + \left(\frac{b}{B_{\text{NP}}} \right)^2} \right)^{-1}, \quad B_{\text{NP}} = 2 \text{ GeV}^{-1}. \quad (3.12)$$

Here $\mathcal{D}_{\text{resum}}$ is the resummed expression for \mathcal{D} at small- b [42] with NNLO perturbative coefficients [43, 44]. The function b^* is such that $b^* \sim b$ at $b \rightarrow 0$ and $b^* \sim 2 \text{ GeV}^{-1}$ at $b \rightarrow \infty$, smoothly passing from the perturbative to non-perturbative regions in b -space and freezing the value of $\mathcal{D}_{\text{resum}}$ before it hits the Landau pole. The parameter B_{NP} has been fixed at 2 GeV^{-1} following these considerations from the SV19 fit: (i) B_{NP} is strongly anti-correlated with c_0 , (ii) its natural values are around $2 \pm 0.3 \text{ GeV}^{-1}$. Given this, we leave only the value c_0 to be fitted from the data. The model in eqn. (3.11) is linear at $b \rightarrow \infty$; this ansatz is partially supported by recent theoretical studies [45, 46] and also in general agreement with the latest lattice computations [47–49]. In refs. [36, 50], models with quadratic asymptotic behavior (as in the studies [51–53]) and with constant asymptotic behavior (in the spirit of the s -channel picture [54–56]) have also been analyzed. Investigations based on these different asymptotic behaviors are left to future work.

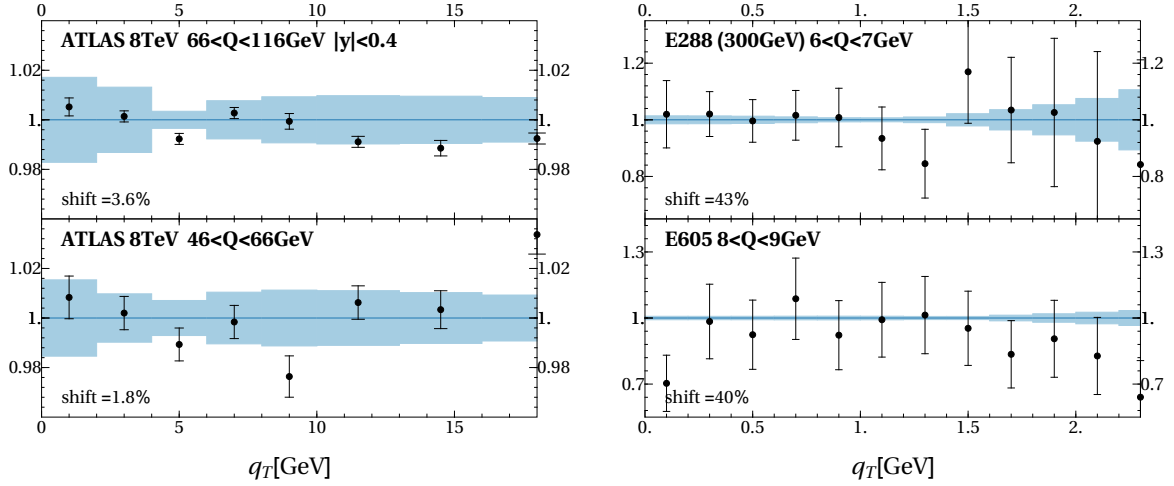


Figure 4: Scale variation band in comparison to typical data at high (left panel) and low (right panel) energies. The scale variation band is defined as the maximum symmetrized deviation from varying all scale parameters by a factor $c \in [0.5, 2]$.

The model for the optimal TMDPDF is

$$f_{1,f \leftarrow h}(x, b) = \sum_{f'} \int_x^1 \frac{dy}{y} C_{f \leftarrow f'}(y; \mu_{\text{OPE}}) q_{f'} \left(\frac{x}{y}, \mu_{\text{OPE}} \right) f_{\text{NP}}^f(x, b), \quad (3.13)$$

where $C_{f \leftarrow f'}$ is the matching coefficient taken at NNLO [57], $q_{f'}$ is the unpolarized PDF of parton f' , and f_{NP} is the NP part to be fitted. The collinear factorization scale μ_{OPE} in the r.h.s. of eqn. (3.13) is taken as

$$\mu_{\text{OPE}} = \frac{2e^{-\gamma_E}}{b} c_4 + 2 \text{ GeV}, \quad (3.14)$$

so that the logarithms $\ln(\mu b/2e^{-\gamma_E})$ present in the matching coefficient vanish at $b \rightarrow 0$ and $c_4 = 1$, and freeze at large- b , before the Landau pole.

In total there are two¹ free scale parameters in our implementation of the TMD factorization – the hard factorization scale μ (3.8), and the scale of small- b matching μ_{OPE} (3.14). To test the stability of the prediction, we vary these scales by factors $c_{2,4}$ in the range $[0.5, 2]$, and take the maximum symmetrized deviation. Note that in our implementation of the c_4 parameter, its variation does not significantly impact the TMDPDFs at $b \gtrsim 4 \text{ GeV}^{-1}$, where perturbation theory cannot be applied. The resulting bands are drawn in fig. 4. They have a typical size of 1-1.5% at $Q \sim M_Z$ and 2-3% at $Q \sim 6 \text{ GeV}$. The largest contribution to the theoretical error comes from the variation of c_4 , in μ_{OPE} . In order to reduce this error one should consider the matching of TMD to PDF at one higher perturbative order, that is N³LO. While perturbative calculations are in principle available [18, 58–60], we use the evolution of PDF as provided by each PDF extraction, which is currently limited at NNLO for all groups. With this choice we have a fully consistent cancellation of logarithms up to NNLO.

The main new feature of the present analysis is the ansatz for the f_{NP} . It is

$$f_{\text{NP}}^f = \exp \left(- \frac{(1-x)\lambda_1^f + x\lambda_2^f}{\sqrt{1+\lambda_0 x^2 b^2}} b^2 \right), \quad (3.15)$$

with $\lambda_{1,2}^f > 0$ and $\lambda_0 > 0$. This is a simplified form with respect to the ansatz used in SV19, but the flavor dependence is original. The model is characterized by an exponential asymptotic fall at $b \rightarrow \infty$ and a

¹There is a third scale associated with the small- b matching of the CS-kernel. In the present implementation it is implicit, and is a part of definition $\mathcal{D}_{\text{resum}}$. Effectively, this scale is $\mu_0 \sim 1/b$. Since the resummation formula is exact, this hidden scale cannot be varied.

Gaussian-like shape at intermediate b . The factor λ_0 accompanying x^2 comes from SV19 (where the fitted power of x was found to be 2.05 ± 0.25) and is also consistent with the general pattern [61] of b power corrections to TMDPDF $\sim (xb)^2$. The parameter λ_0 is universal for all flavors.

The parameters $\lambda_{1,2}$ are taken to be flavor dependent. We distinguish u, d, \bar{u}, \bar{d} and *sea* cases, where *sea* is used for $(s, \bar{s}, c, \bar{c}, b, \bar{b})$ flavors. In total we have 11 free parameters. Since the parameters $\lambda_{1,2}$ are almost uncorrelated in-between flavors, the presence of unnecessary fitting parameters (i.e. not well restricted in a particular setup) does not lead to an overfit.

The numerical implementation is made with `artemide` [5], which can be found in open-access repository [62]. The PDF values and their evolution are taken from the LHAPDF [63]. `Artemide` is written in FORTRAN, with a Python interface. The evaluation of a single DY-cross-section point includes two convolutions of PDF, Hankel type integrals and three integrations over the phase space. Additionally, for some measurement one needs to compute the factor \mathcal{P}_1 . The `artemide` code is optimized for such computations, and it uses various numerical tricks, such as precomputed grids, specially optimized integration algorithms, parallel evaluation. Even so the computation of one value of χ^2 for the data set takes from 30 seconds to a few minutes, depending on the PDF input, NP parameters and hardware. Therefore, a single minimisation procedure (made with the help of iMINUIT package [64]) requires typically a few dozen hours on an average computer. This was the main complication of the present study, which required the run of minimization several thousands times.

4 TMD data sets

4.1 Complete data set

The complete data set used in this study is given in tab. 1. It is almost identical to the one used for the analysis [3], with the only addition of the recent CMS Z-boson production data at 13 TeV ² [65]. As in several recent studies (see e.g. refs. [4–6]), we restrict the fit to data points in the low transverse momentum region by implementing the cut $q_T/Q < 0.25$ ³. In addition we implement an extra cutting rule for the very precise data typically encountered at LHC. Given a data point $p(1 \pm \sigma)$, with p being the central value and σ its uncorrelated relative uncertainty, corresponding to some values of q_T and Q , we include it in the fit only if

$$\delta \equiv \frac{\langle q_T \rangle}{\langle Q \rangle} < 0.1, \quad \text{or} \quad \delta < 0.25 \quad \text{if} \quad \delta^2 < \sigma. \quad (4.1)$$

In other words, if the (uncorrelated) experimental uncertainty of a given data point is smaller than the theoretical uncertainty associated to the expected size of the power corrections, we drop it from the fit.

The resulting data set in tab. 1 contains 507 data points, and spans a wide range in mass, from $Q = 4$ GeV to $Q = 150$ GeV, and in x , from $x \sim 0.5 \cdot 10^{-4}$ to $x \sim 1$. The data roughly split into low-energy and high-energy points. The low-energy subset contains data from fixed target experiments E288 [66], E605 [67] and E772 [68], and PHENIX [69]. The high-energy subset contains data from the neutral current DY (Z/ γ -boson) measured at Tevatron and LHC by different detectors. The subsets have similar number of points but those in the high-energy subset are one order of magnitude more precise. The data that we are using are very similar to those included in previous fits [3, 4, 6].

The treatment of particular aspects of the measurements such as bin-integration, nuclear modifications and normalization conditions are as in ref. [3] and we refer to this for extra details. Notice that we use the absolute values of the cross-section, whenever available, and perform the full bin-integration to accurately incorporate the phase-space effects. The only modification of the data treatment in comparison to [3] is the splitting of the low-energy measurements (namely E288 at $E_{\text{beam}} = 300$ and 400 GeV, E605 and E772) into two independent subsets below and above the Υ -resonance. This allows us to treat the normalization error independently for these energies. The reason for doing this is a possible inconsistency between these energy regions inside the measurements, which leads to tensions.

²We learned about these data when the main fit had already been made. Therefore, the CMS Z-boson production data at 13 TeV are not included in the fit but only in the comparisons.

³Treating the region $q_T \sim Q$ requires the inclusion of power corrections in q_T/Q or matching with finite-order (NLO or NNLO) hard scattering coefficients.

Experiment	ref.	\sqrt{s} [GeV]	Q [GeV]	y/x_F	N_{pt} after TMD cuts	N_{pt} in red.set
E288 (200)	[66]	19.4	4 - 9 in 1 GeV bins*	$0.1 < x_F < 0.7$	43	39
E288 (300)	[66]	23.8	4 - 12 in 1 GeV bins*	$-0.09 < x_F < 0.51$	53	53
E288 (400)	[66]	27.4	5 - 14 in 1 GeV bins*	$-0.27 < x_F < 0.33$	76	76
E605	[67]	38.8	7 - 18 in 5 bins*	$-0.1 < x_F < 0.2$	53	53
E772	[68]	38.8	5 - 15 in 8 bins*	$0.1 < x_F < 0.3$	35	24
PHENIX	[69]	200	4.8 - 8.2	$1.2 < y < 2.2$	3	2
CDF (run1)	[70]	1800	66 - 116	inclusive	33	0
CDF (run2)	[71]	1960	66 - 116	inclusive	39	15
D0 (run1)	[72]	1800	75 - 105	inclusive	16	0
D0 (run2)	[73]	1960	70 - 110	inclusive	8	0
D0 (run2) $_{\mu}$	[74]	1960	65 - 115	inclusive	3	3
ATLAS (7TeV)	[75]	7000	66 - 116	$ y < 1$ $1 < y < 2$ $2 < y < 2.4$	15	0
ATLAS (8TeV)	[76]	8000	66 - 116	$ y < 2.4$ in 6 bins	30	30
ATLAS (8TeV)	[76]	8000	46 - 66	$ y < 2.4$	3	3
ATLAS (8TeV)	[76]	8000	116 - 150	$ y < 2.4$	7	0
CMS (7TeV)	[77]	7000	60 - 120	$ y < 2.1$	8	0
CMS (8TeV)	[78]	8000	60 - 120	$ y < 2.1$	8	0
CMS (13TeV)	[65]	13000	76 - 106	$ y < 2.4$ in 6 bins	50	0**
LHCb (7TeV)	[79]	7000	60 - 120	$2 < y < 4.5$	8	4
LHCb (8TeV)	[80]	8000	60 - 120	$2 < y < 4.5$	7	7
LHCb (13TeV)	[81]	13000	60 - 120	$2 < y < 4.5$	9	0
Total					507	309

*Bins with $9 \lesssim Q \lesssim 11$ are omitted due to the Υ resonance.

Table 1: Summary table for the data included in the fit. For each data set we report: reference publication, centre-of-mass energy, coverage in Q and y or x_F , possible cuts on the fiducial region, and number of data points that survive the cut in eqn. (4.1).

4.2 Reduced data set

Given the data set defined above, we observe that the sensitivity to NP parameters of the TMD distributions varies strongly within the data set. For instance, data points with $q_T \sim 15 - 25$ GeV have little power in constraining NP parameters, irrespective of their precision, because they are deeply inside the resummation region, where the Hankel integral is dominated by the $b \ll 1\text{GeV}^{-1}$ contribution, and determined by PDF values only. The inclusion of these points in the fit is not harmful but rather time consuming. To speed up the fitting procedure, we have considered a reduced set of data points.

To identify the relevant points for the TMD extraction, we tested the sensitivity of the theory prediction to the variation of NP parameters, and included only the points that are sensitive to the variation. Given a NP parameter p , we compute the cross-section for several values of p distributed in the range $p \pm \delta p$, and compute the sensitivity coefficient between p and the cross-section, by the formula

$$s_{\sigma,p} = \frac{\langle \sigma \cdot p \rangle - \langle \sigma \rangle \langle p \rangle}{\Delta \sigma \delta p}, \quad (4.2)$$

where $\Delta\sigma$ is the uncorrelated experimental uncertainty of the point. The sensitivity coefficient indicates how strongly a prediction for a data point depends on the parameter p . E.g., $s_{\sigma,p} = 1$ means that the variation of p by δp gives rise to a variation in the theory prediction equal to the experimental uncertainty.

We computed the sensitivity coefficient for each point in the data set and for each parameter of our NP ansatz. The values of δp are taken using the Hesse estimation for its uncertainty multiplied by a factor 5. Points with $s > 0.4$ for at least one parameter were included in the reduced set. This test was run for each of the PDF sets that we studied, and the union of data was taken. This provided us with a very conservative selection of impacting data.

Afterwards, we excluded the sets with too few points, such as LHCb (13 TeV) (1 surviving point) and CDF (run1) (5 points remaining out of 33). Additionally, we excluded the ATLAS (7 TeV) measurement since it has shown an anomalous behaviour and provides significant tension with other similar measurements⁴.

The reduced set contains 309 data points. Most excluded points are from the region characterized by high energy and high q_T . The low-energy subset, in contrast, is very sensitive to the NP input and lost only 15 points due to their large error bands. We have checked, by evaluating several random cases, that the minimum of the χ^2 computed with the reduced set almost coincides (up to 2 digits) with the minimum of the global set. Simultaneously, the computation for the reduced set is about three times faster, which facilitates the analysis.

5 Statistical framework

The central point of the present study is the impact of the PDF uncertainty on the extraction of TMD distributions. Therefore, we distinguish two sources of uncertainties: *i*) the experimental uncertainties and *ii*) the uncertainty of the collinear PDFs. These have different nature, and could not be easily combined together. In fact, the best approach to account for the PDF uncertainty would be a simultaneous global fit of collinear PDF and TMDPDF, which is challenging. In the present work, we use the strategy of combining PDF and experimental uncertainty based on Bayesian statistics, described in this section.

5.1 Definition of the χ^2 -function

Our main tool is the χ^2 -test function, which estimates the goodness of a theory prediction. It is defined as

$$\chi^2 = \sum_{i,j=1}^n (m_i - t_i) V_{ij}^{-1} (m_j - t_j), \quad (5.1)$$

where i and j enumerate points of the data set. For the i th point, t_i is the corresponding theoretical prediction, m_i is the experimental value, and all the information about the uncertainties for individual data points and the relation between them is given by the covariance matrix V_{ij} . The definition of V_{ij} is crucial for an adequate analysis of the data and interpretation of the results. Its construction distinguishes two types of uncertainties: uncorrelated and correlated. In general, the i th point is given as

$$m_i \pm \sigma_{i,\text{stat}} \pm \sigma_{i,\text{unc}} \pm \sigma_{i,\text{corr}}^{(1)} \pm \dots \pm \sigma_{i,\text{corr}}^{(k)}. \quad (5.2)$$

Here $\sigma_{i,\text{stat}}$ and $\sigma_{i,\text{unc}}$ are the uncorrelated statistical and systematic uncertainties, respectively, that estimate the degree of knowledge of the i th data point regardless of all other data in the set. The correlated uncertainties $\sigma_{i,\text{corr}}^{(k)}$ (with $k = 1, \dots, n$) estimate the relation between the statistical fluctuations of the i th point and all others in the set. The covariance matrix V_{ij} can be written as [82, 83]

$$V_{ij} = (\sigma_{i,\text{stat}}^2 + \sigma_{i,\text{unc}}^2) \delta_{ij} + \sum_{l=1}^k \sigma_{i,\text{corr}}^{(l)} \sigma_{j,\text{corr}}^{(l)}, \quad (5.3)$$

Using this expression in the computation of eqn. (5.1) allows us to reach the reliable estimation of data-to-theory agreement, while taking into account the nature of experimental uncertainties.

⁴The same observation was also made by the PDF fitting collaborations NNPDF [23] and CT-TEA [22], which exclude these data from the pool.

The minimum of the χ^2 -test function determines the preferred values of the NP parameters λ , which in turn characterize the preferred shape of TMD distributions. The fit procedure consists in the minimization of χ^2 , which is performed with the iMinuit package [64].

In fitting a multivariate function one usually finds several sets of parameters giving numerous local minima of the function. Some of these give mathematically correct but physically unsound results, and therefore a strategy should be implemented to discard them. The MINUIT algorithm can handle the problem of choosing the correct minimum, unless the minima are significantly separated in the parameter space and/or the step (the amount by which the parameters move in one iteration) is too small. In our case, with the χ^2 -function depending on 11 parameters, we have faced the problem of the minimisation algorithm selecting a definitely unphysical minimum. Each occurrence is characterized by values of parameters that (almost) suppress a contribution of some flavor.

In order to disregard such contributions we introduced penalty terms into the minimisation function. The penalty function is defined as

$$P(\lambda) = 10^{-2} \left(r(\lambda_1^u, \lambda_1^d) + r(\lambda_2^u, \lambda_2^d) + r(\lambda_1^{\bar{u}}, \lambda_1^{\bar{d}}) + r(\lambda_2^{\bar{u}}, \lambda_2^{\bar{d}}) \right), \quad (5.4)$$

where

$$r(a, b) = \begin{cases} x - 1, & x > 1 \\ 0, & \text{otherwise,} \end{cases} \quad \text{with } x = \max\left(\frac{a}{b}, \frac{b}{a}\right). \quad (5.5)$$

This function is non-zero only if the parameters of the u/d and \bar{u}/\bar{d} distributions differ from each other by an order of magnitude. So, the minimisation was performed for the function

$$X(\text{data}, \text{PDF}; \lambda) = \chi^2 + P(\lambda). \quad (5.6)$$

5.2 Input PDFs and their uncertainties

Four PDF sets were used in our study, the bold font denoting the shorthand name used to identify them in the rest of this article:

- **HERA20**. The NNLO extraction by the H1 and ZEUS collaborations presented in ref. [20] with Hesse-like error band. The LHAPDF entry is `HERAPDF20_NNLO_VAR` with id = 61230.
- **NNPDF31**. The NNLO extraction by the NNPDF collaboration presented in ref. [23] with 1000 replicas at $\alpha_s(M_Z) = 0.118$. The LHAPDF entry is `NNPDF31_nnlo_0118_1000` with id = 309000.
- **CT18**. The NNLO extraction by the CTEQ collaboration presented in ref. [22] with Hesse error band. The LHAPDF entry is `CT18NNLO` with id = 14000.
- **MSHT20**. The NNLO extraction by the MSHT collaboration presented in ref. [21] with Hesse error band. The LHAPDF entry is `MSHT20nnlo_as118` with id = 27400.

The comparison of these PDFs for u - and d -quarks at scale $\mu = 2$ GeV is presented in Fig. 1.

In what follows the analyses are done using Bayesian statistics, which requires representing the PDFs as Monte-Carlo (MC) ensembles. As the **NNPDF31** set is already given in this form, no further pre-processing is required. The other three distributions have a Hessian definition of uncertainty bands. The corresponding MC ensembles are generated using the prescription given in ref. [84]. Namely, for a distribution $f(x)$ with 68% C.I. for each eigenvector given by f_i^\pm ($i = 1, \dots, D$, with f_i^+ and f_i^- the upper and lower bounds, respectively), a MC replica is generated by

$$f^{(k)}(x) = \sum_{i=1}^D \left(\frac{f_i^+(x) - f_i^-(x)}{2} R_i^{(k)} + \frac{f_i^+(x) + f_i^-(x) - 2f(x)}{2} \left(R_i^{(k)} \right)^2 \right), \quad (5.7)$$

where $R_i^{(k)}$ is a univariate random number. Using this method we generated 1000 MC replicas for **HERA20**, **CT18** and **MSHT20**, which were used in the analyses. We have checked that the uncertainty bands obtained from the generated MC replicas are almost identical to the original Hesse uncertainty bands. The comparison of uncertainty bands for different PDF is given in fig.1.

5.3 Determination of uncertainties & presentation of the result

Within Bayesian statistics, the propagation of uncertainties to the free parameters is made by fitting each member of the input ensemble. Our input ensemble is generated accounting for two independent sources of uncertainty:

EXP: The experimental uncertainty is accounted for by generating pseudo-data. A replica of the pseudo-data is obtained adding Gaussian noise to the values of the data points (and scaling the uncertainties if required). The parameters of the noise are dictated by the correlated and uncorrelated experimental uncertainties. The procedure is described in ref. [82]. We considered such 100 replicas.

PDF: The uncertainty due to the collinear PDF is accounted for by using each PDF replica as input. We considered 1000 replicas generated as described in sec. 5.2.

The number of pseudo-data replicas is lower because the resulting uncertainty is much smaller than the one coming from the PDF distribution, as demonstrated in the following.

Fitting each member of the ensemble, we end up with the two-dimensional set λ_{ij} , where λ is a 11-dimensional vector of fitting parameters (including $\lambda_{1,2}^f$, λ_0 and c_0), i runs over the pseudo-data replicas, and j runs over the PDF replicas. This set is distributed in accordance to the experimental and PDF uncertainties propagated through our fitting procedure. Due to the computational limitations mentioned in subsec. 3.2, calculating the full distribution with $100 \times 1000 = 10^5$ members is unrealistic. To simplify the task, we consider two distributions. The first one, labeled **EXP**, when the replicas of the data are fitted with the central PDFs. The second one, called **PDF**, when the replicas of the PDFs are fitted with the central (original) data. Symbolically,

$$\{\lambda\}_{\mathbf{PDF}} = \bigcup_{j=1}^{N_{\text{rep,PDF}}} \lambda_{0j}, \quad \{\lambda\}_{\mathbf{EXP}} = \bigcup_{i=1}^{N_{\text{rep,data}}} \lambda_{i0}, \quad (5.8)$$

where $i = 0$ indicates the replica with unmodified data, and $j = 0$ a replica computed with the central value of the PDF.

The **PDF** and **EXP** distributions are treated as independent. These are not Gaussian, in particular the **PDF** case, in which the distributions are also notably non-symmetric. Therefore, we estimate the 68% C.I. for a parameter using the bootstrap method. Namely, we compute the [16%, 84%] quantile for a large number of samples and take the average interval. The results are presented as $a_{\delta a_1}^{\delta a_2}$, where a is the mean value of the parameter and δa 's are the distances to the 68% C.I. boundary.

A drawback of performing the fit independently for each case is the appearance of several issues when wanting to join the two forms in a single meaningful one. The main problem is that, for some parameters, the distance between the mean values of the distributions is large. This renders impossible any naive description of a joined distribution; for example, the average value of the extracted TMDPDFs would have a large χ^2 , meaning that the corresponding TMDPDFs would not provide an adequate description of the data. Lesser, but not unimportant, problems are the correlations between individual points of TMDPDFs, and the PDF bias of the **EXP** case. Therefore, finally we present the central value and the 68% C.I., computed as described below.

The central value of our fit is obtained as the TMDPDF computed with the central values of the PDFs and NP parameters. The latter are computed as the weighted average of the **PDF** and **EXP** cases,

$$a = w_{\mathbf{PDF}} \langle \{a\}_{\mathbf{PDF}} \rangle + w_{\mathbf{EXP}} \langle \{a\}_{\mathbf{EXP}} \rangle, \quad w_i = \frac{\sigma_i^{-2}}{\sigma_{\mathbf{PDF}}^{-2} + \sigma_{\mathbf{EXP}}^{-2}}, \quad (5.9)$$

where $i = \mathbf{PDF}$ or **EXP**, and $\sigma_i = (\delta a_{1i} - \delta a_{2i})/2$ is the half-size of the 68% C.I.. In this way, the central value incorporates information from both cases but retains the knowledge of which case gives a better determination of the considered parameter. The final parameters obtained by this procedure for each PDF set are shown in tab. 4. Also, the central distribution so defined returns a reasonable value of χ^2 , which should be similar to the result that we would obtain if we had performed one joined fit. The joined 68% C.I., instead, is computed from the (equal weight) sum of replicas distributions, $\{\lambda\}_{\text{joined}} = \{\lambda\}_{\mathbf{PDF}} \cup \{\lambda\}_{\mathbf{EXP}}$ by a bootstrap method.

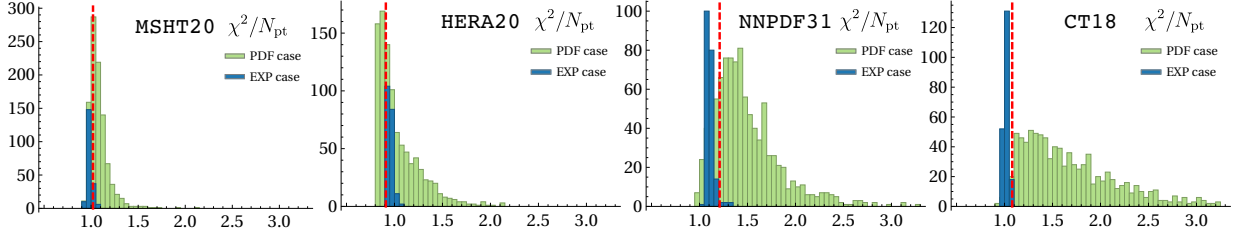


Figure 5: Distribution of χ^2 -values for the **PDF** and **EXP** cases. The red lines show the position of the final χ^2 -value.

Data set	N_{pt}	MSHT20	HERA20	NNPDF31	CT18
		χ^2/N_{pt}	χ^2/N_{pt}	χ^2/N_{pt}	χ^2/N_{pt}
CDF run2	15	0.96	0.68	0.65	0.82
D0 run2 (μ)	3	0.50	0.59	0.55	0.52
ATLAS 8TeV $0.0 < y < 0.4$	5	2.97	3.66	2.12	3.23
ATLAS 8TeV $0.4 < y < 0.8$	5	2.00	1.53	4.52	3.21
ATLAS 8TeV $0.8 < y < 1.2$	5	1.00	0.50	2.75	1.89
ATLAS 8TeV $1.2 < y < 1.6$	5	2.25	1.61	2.49	2.72
ATLAS 8TeV $1.6 < y < 2.0$	5	1.92	0.68	2.86	1.96
ATLAS 8TeV $2.0 < y < 2.4$	5	1.35	1.14	1.47	1.06
ATLAS 8TeV $46 < Q < 66 \text{ GeV}$	3	0.59	1.86	0.23	0.05
LHCb 7TeV	4	3.19	0.34	2.58	1.68
LHCb 8TeV	7	1.38	1.29	1.63	0.83
PHE200	2	0.32	0.36	0.43	0.27
E228-200	39	0.44	0.38	0.51	0.45
E228-300 $Q < 9 \text{ GeV}$	43	0.77	0.56	0.89	0.55
E228-300 $Q > 11 \text{ GeV}$	10	0.29	0.37	0.45	0.44
E228-400 $Q < 9 \text{ GeV}$	34	2.19	1.15	1.49	1.34
E228-400 $Q > 11 \text{ GeV}$	42	0.25	0.61	0.44	0.40
E772	24	1.58	1.92	2.51	1.56
E605 $Q < 9 \text{ GeV}$	21	0.52	0.47	0.47	0.61
E605 $Q > 11 \text{ GeV}$	32	0.47	0.73	1.34	0.52
Total	309	0.97	0.85	1.17	0.87

Table 2: Distribution of the values of χ^2 over the reduced data set in fits with different PDF inputs.

The same procedure is also carried out for the values of cross-section presented in the next section. I.e. the values of cross-section are computed for all members of $\{\lambda\}_{\text{PDF}}$ and $\{\lambda\}_{\text{EXP}}$ resulting into $\{\sigma\}_{\text{PDF}}$ and $\{\sigma\}_{\text{EXP}}$. Then the central values and the 68% C.I. are computed using the same strategy. This procedure (rather than computation of average values of parameters) accounts for the correlation between different values of TMDPDFs.

6 Results & discussion

6.1 Agreement between data and theory

The individual values of χ^2 for each experiment obtained for the reduced and complete data sets are given in tabs. 2 and 3, respectively. The tables also report the total χ^2 of the fits. As expected, the value of χ^2/N_{pt} for the reduced data set is better than the one for the whole set, but the differences do not appear to be significant. The main conclusion we can draw from these quantities is that the differences observed in previous fits such as SV19 [3] when using different PDF sets are substantially reduced. Now, instead, a reasonable description of the data is achieved with all PDF sets.

The χ^2 distribution among the **PDF** and **EXP** replicas is shown in fig. 5. In general they are consistent with each other and their spread is highly reduced with respect to previous fits, including SV19. This confirms the relevance of inserting flavor dependence into f_{NP} . For all cases the **PDF** replicas provide a much larger dispersion of the χ^2 values than the **EXP** ones. The shapes of χ^2 -distributions are visibly different for different collinear PDFs, despite the resulting uncertainties in cross-section and TMDPDFs

Data set	N_{pt}	MSHT20	HERA20	NNPDF31	CT18
		χ^2/N_{pt}	χ^2/N_{pt}	χ^2/N_{pt}	χ^2/N_{pt}
CDF run1	33	0.78	0.61	0.72	0.75
CDF run2	39	1.70	1.42	1.68	1.79
D0 run1	16	0.71	0.81	0.79	0.79
D0 run2	8	1.95	1.39	1.92	2.00
D0 run2 (μ)	3	0.50	0.59	0.55	0.52
ATLAS 7TeV $0.0 < y < 1.0$	5	4.06	1.94	2.12	4.21
ATLAS 7TeV $1.0 < y < 2.0$	5	7.78	4.83	4.52	6.12
ATLAS 7TeV $2.0 < y < 2.4$	5	2.57	2.18	3.65	2.39
ATLAS 8TeV $0.0 < y < 0.4$	5	2.98	3.66	2.12	3.23
ATLAS 8TeV $0.4 < y < 0.8$	5	2.00	1.53	4.52	3.21
ATLAS 8TeV $0.8 < y < 1.2$	5	1.00	0.50	2.75	1.89
ATLAS 8TeV $1.2 < y < 1.6$	5	2.25	1.61	2.49	2.72
ATLAS 8TeV $1.6 < y < 2.0$	5	1.92	1.68	2.86	1.96
ATLAS 8TeV $2.0 < y < 2.4$	5	1.35	1.14	1.47	1.06
ATLAS 8TeV $46 < Q < 66 \text{ GeV}$	3	0.59	1.86	0.23	0.05
ATLAS 8TeV $116 < Q < 150 \text{ GeV}$	7	0.61	1.03	0.85	0.70
CMS 7TeV	8	1.22	1.19	1.30	1.25
CMS 8TeV	8	0.78	0.77	0.75	0.78
CMS 13TeV $0.0 < y < 0.4$	8	3.52	1.93	2.13	3.73
CMS 13TeV $0.4 < y < 0.8$	8	1.06	0.53	0.71	1.65
CMS 13TeV $0.8 < y < 1.2$	10	0.48	0.14	0.33	0.88
CMS 13TeV $1.2 < y < 1.6$	11	0.62	0.33	0.47	0.86
CMS 13TeV $1.6 < y < 2.4$	13	0.46	0.32	0.39	0.57
LHCb 7TeV	8	1.79	1.00	1.62	1.16
LHCb 8TeV	7	1.38	1.29	1.63	0.83
LHCb 13TeV	9	1.28	0.84	1.07	0.93
PHE200	3	0.29	0.42	0.38	0.29
E228-200	43	0.43	0.36	0.57	0.43
E228-300 $Q < 9 \text{ GeV}$	43	0.77	0.56	0.89	0.55
E228-300 $Q > 11 \text{ GeV}$	10	0.29	0.37	0.45	0.44
E228-400 $Q < 9 \text{ GeV}$	34	2.19	1.15	1.49	1.34
E228-400 $Q > 11 \text{ GeV}$	42	0.25	0.61	0.44	0.40
E772	35	1.14	1.37	1.79	1.11
E605 $Q < 9 \text{ GeV}$	21	0.52	0.47	0.47	0.61
E605 $Q > 11 \text{ GeV}$	32	0.47	0.73	1.34	0.52
Total	507	1.12	0.91	1.21	1.08

Table 3: Distribution of the values of χ^2 over the TMD data set in fits with different PDF input.

being similar. We suppose that this is due to the complexity of the corresponding parametrizations. In particular, the NNPDF and CT18 cases have more disturbed shapes of individual replicas (in comparison to HERA20 and MSHT20 cases) and consequently a larger spread of the χ^2 distribution.

The quality achieved in describing the data within the present fit is illustrated in figs. 6 and 7, for different PDF cases. Given the variety of experiments included in the fit and the number of PDF sets used, we present here only a fraction of all results obtained. We refer the interested reader to the supplementary material for the complete collection of plots. The left panel of fig. 6 illustrates the Z-boson production measured by ATLAS at $\sqrt{s} = 8 \text{ TeV}$ [76], the most precise data set in our analysis. On the right panel of fig. 6, we show the comparison of the theory prediction to data for the Z-boson production measured by CMS at $\sqrt{s} = 13 \text{ TeV}$ [65]. Notice that these data were not included in the fit. As an example of the lowest energy measurements considered in the analysis, we present in Fig. 7 the DY-process measured by the E288 experiment [66]. In all cases, the **PDF**-uncertainty is larger than the **EXP**-uncertainty. This is especially pronounced for the high-energy measurements, for which the experimental uncertainty is small, and thus the uncertainty band is dominated by the **PDF** error. For $q_T \gtrsim 10 \text{ GeV}$, the **EXP**-uncertainty became negligible since this is the resummation regime, insensitive to the non-perturbative TMD effects. In a few cases (central rapidity Z-boson production with CT18, and the lowest energy bins for DY process with NNPDF3.1), the **PDF** and **EXP** bands do not overlap, which demonstrate an unrevealed tension in the fitting procedure.

The important observation is that the resulting uncertainty band can be larger than the experimental uncertainties. It happens for the precise ATLAS measurements and several low-energy measurements. It

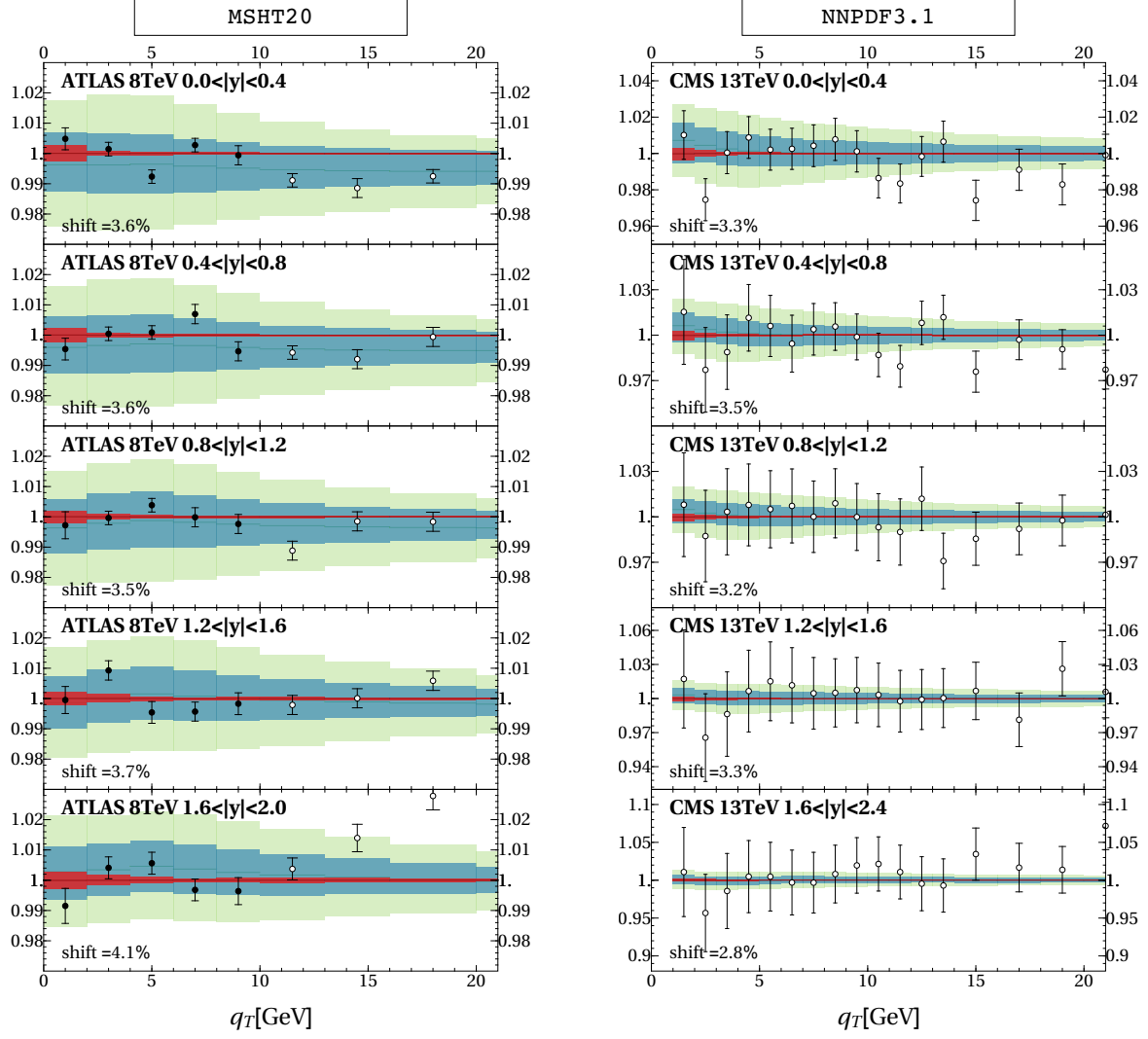


Figure 6: Example of the data description at high energy. Left panel: the ratio $d\sigma_{\text{experiment}}/d\sigma_{\text{theory}}$ for Z-boson production at 8 TeV measured by the ATLAS experiment with MSHT20. Right panel: the ratio $d\sigma_{\text{experiment}}/d\sigma_{\text{theory}}$ for Z-boson production at 13 TeV at the CMS experiment with NNPDF3.1. The red band is the **EXP**-uncertainty. The light-green band is the **PDF**-uncertainty. The blue band is the combined uncertainty. Only the filled bullets are included into the fit.

also indicates that including these measurements in the joined fit of PDFs and TMDPDFs will put extra constraints on the PDFs. Therefore, we conclude that the PDF uncertainty in the TMD approach cannot be neglected under any circumstances.

6.2 Extracted TMD distributions

Another important piece of information comes from the values and error bars of the fitted parameters. These are given in tab. 4 and plotted in fig. 8. There, we report the bands obtained from the estimation of the **PDF** error (blue), the **EXP** error (red), and the averaged result (black). The central values for the **PDF**, **EXP** and joined cases do not coincide because they are computed with the respective replicas as explained in sec. 5. An outcome of this picture is that there is a general agreement among parameters within error bands. However, each PDF case has a few parameters whose values deviate significantly from the rest. These are $\{\lambda_2^d, \lambda_{1,2}^s\}$ for CT18, $\{\lambda_1^u, \lambda_2^d\}$ for NNPDF3.1, $\{\lambda_2^u, \lambda_2^d\}$ for HERA20, and λ_1^u for MSHT20. This highlights the tension in the corresponding domain between PDF and TMDPDF extractions, and (most probably) it plays a role in the larger values of χ^2 in flavor-independent fits of TMDPDFs. The most striking observation arising from fig. 8 is that the **PDF** error (blue) is generally much larger than the **EXP** error

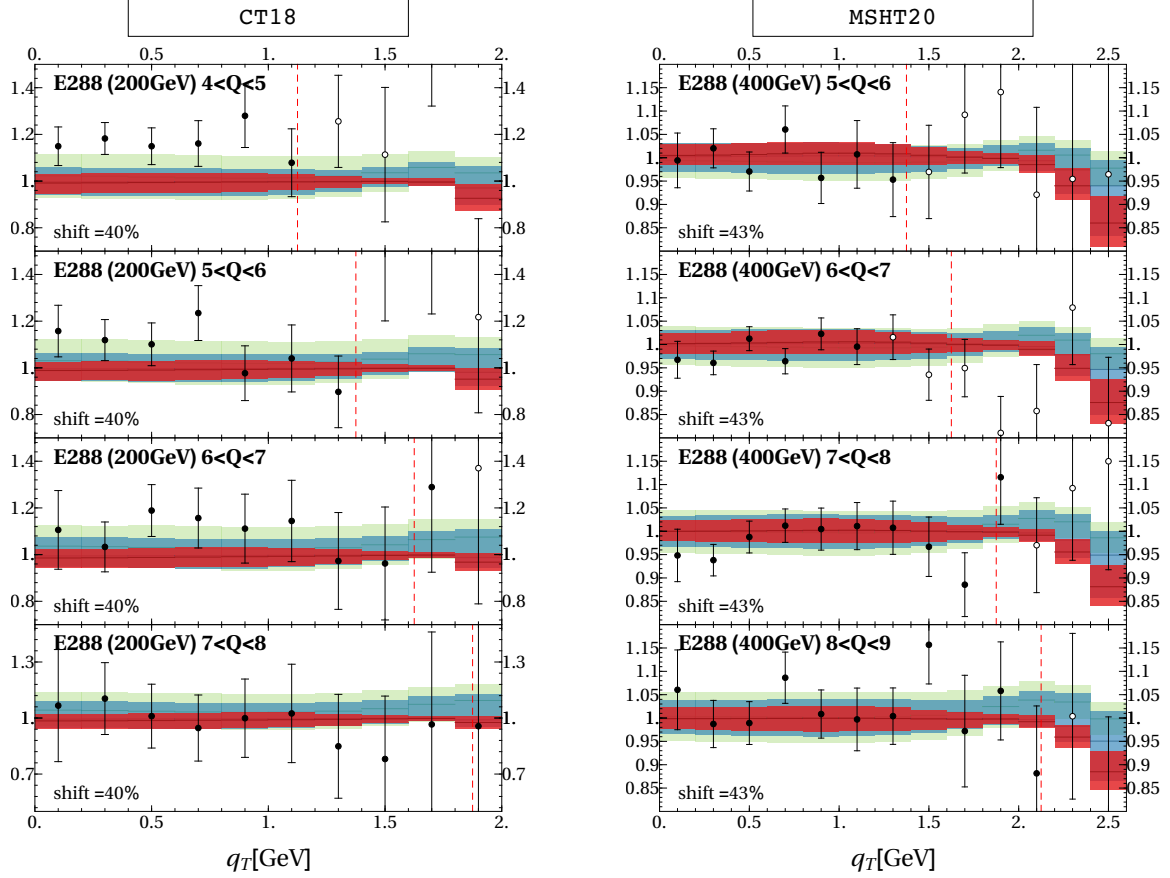


Figure 7: Example of the data description at low energy. Left panel: ratio $d\sigma_{\text{experiment}}/d\sigma_{\text{theory}}$ for the DY process at E288 experiment with 200 GeV beam-energy with CT18. Right panel: ratio $d\sigma_{\text{experiment}}/d\sigma_{\text{theory}}$ for the DY process at E288 experiment with 400GeV beam-energy with MSHT20. Red band is the **EXP**-uncertainty. Light-green band is the **PDF**-uncertainty. The blue band is the combined uncertainty. The filled bullets are included into the fit. The dashed red vertical lines show the expected boundary of the TMD factorization $q_T = 0.25Q$.

(red). In other words, *the error due to a single PDF-set uncertainty is always the most significant*. This aspect may be relevant for future PDF analyses and should be taken into account by future TMDPDF fits.

The fits in refs. [3, 4, 6, 24] have found deficits in the predicted cross sections compared to measurements, with the deficits being small in the case of high-energy measurements (typically, 1-4%) but more significant for low-energy measurements (typically, 30-40%). In most cases, the discrepancy in the normalization is compensated by the correlated uncertainty of the experiment (e.g., E288 measurements have 25% uncertainty due to the beam luminosity), and thus does not significantly increase the value of χ^2 . Each PDF set requires its own normalization factor, e.g. for the central rapidity Z-boson production measured at ATLAS 8 TeV, the deficits are {3.6, 1.4, 2.1, 6.4}% for {MSHT20, HERA20, NNPDF3.1, CT18} cases. Another example is E288 at 200 GeV with {30, 49, 40, 39}% correspondingly. Therefore, the normalization of the cross-section is strongly dependent on the used PDF.

The actual shapes of the extracted TMDPDF are summarized in figs. 9, 10 and 11. Fig. 9 provides the overall picture, while a more detailed view is offered by the slices in b (fig. 10) and x (fig. 11) space, showing the TMDPDF for each PDF set divided by the averaged central value of all PDF cases. The size of the uncertainty changes drastically from the low- b region, where we have a good knowledge of the perturbative expansion, to the completely non-perturbative high- b region (fig. 10). For $b \geq 2 \text{ GeV}^{-1}$ the relative error on the TMD distributions is not less than 60-80%. This is roughly 4-5 times larger than in the SV19 extraction [3]. Also, the present extraction has a non-zero uncertainty band at $b = 0$ which was forbidden by construction in all previous studies.

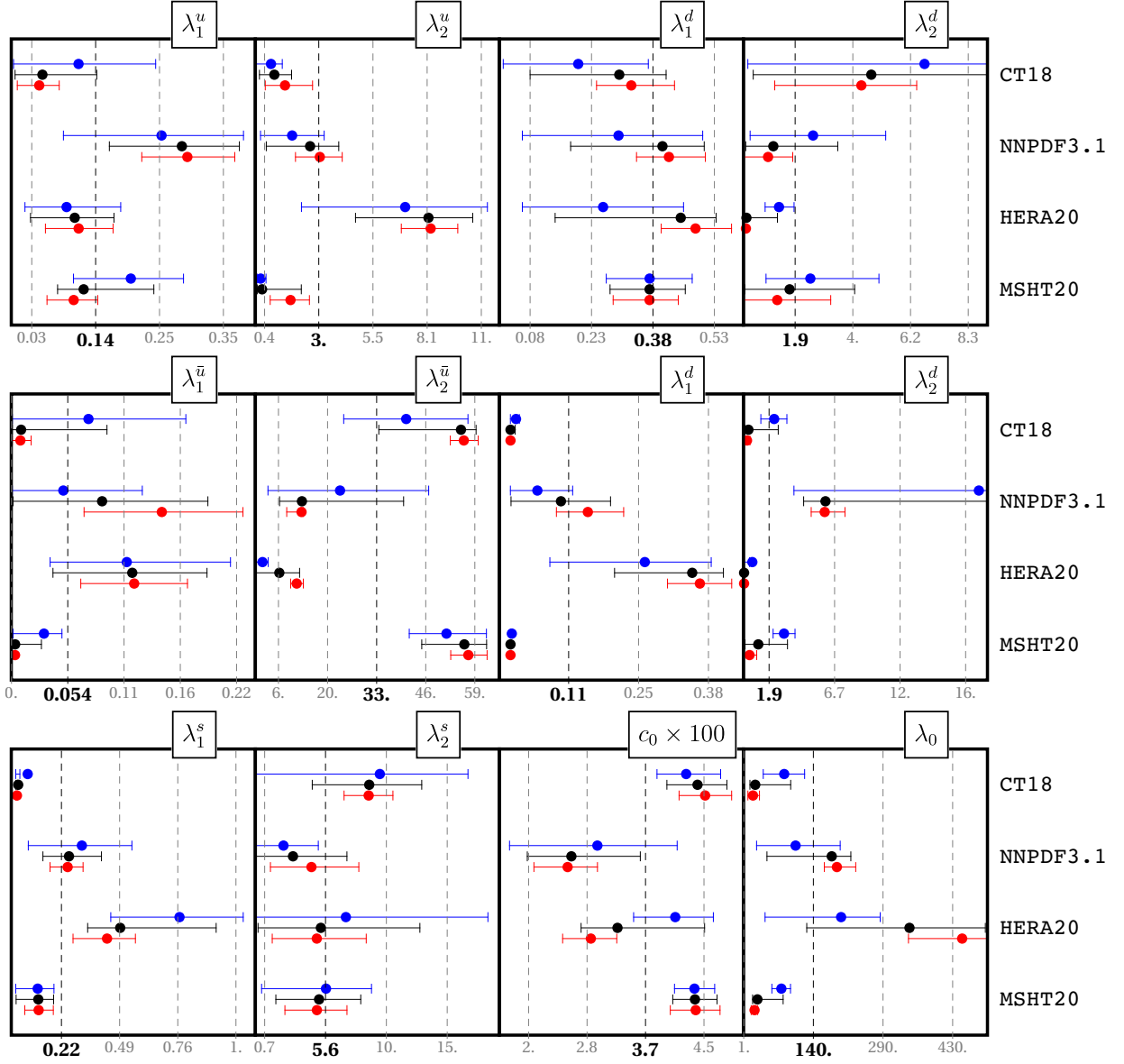


Figure 8: Comparison of the parameter values. Black is the final result. Blue is the value from the fit of the **PDF** case. Red is the value from the fit of the **EXP** case.

Generally, the TMDPDFs extracted with different PDFs display rather diverse behavior. There are a few examples in which TMDPDFs agree at large b despite very different values at $b = 0$, and vice-versa (compare, e.g., the HERA20 and MSHT20 cases for d - and s -quarks). This raises a relevant question, namely, to what extent does the extracted flavor dependence represent the actual dependence, or compensate shortcomings of the collinear PDFs. We are not able to answer this question within the present model for the TMDPDF. The smoothness of the ansatz in eqn. (3.13) leads to a strong correlation between large and small values of b . Only in a few cases we can reliably identify the effect of compensation. For instance, this occurs for the s -quark with CT18 PDF, in which case the central line and the band depart from other extractions, as is also evident from the comparison of fitting parameters. In general, however, we are not able to provide an accurate interpretation in every case.

As an attempt to further study the induced and physical flavor dependence, we have turned to the Mellin moments of the TMDPDFs. We consider the following quantities

$$f_f^{(n)}(b) = \int_{x_{\min}}^1 dx x^{n-1} f_{1,f \leftarrow h}(x, b), \quad (6.1)$$

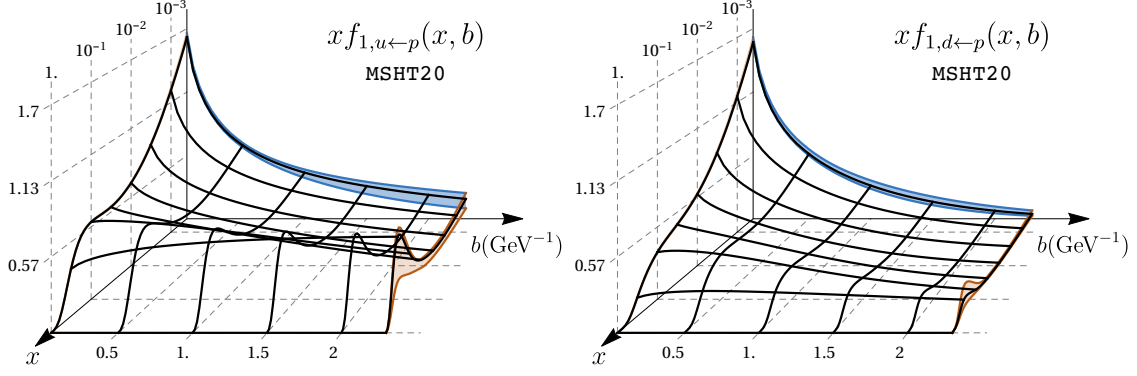


Figure 9: The optimal TMDPDF as a function of (x, b) for u and d quarks with the MSHT20 PDF-input. The uncertainty is demonstrated at boundaries.

where we set $x_{\min} = 10^{-5}$. One may expect that the dependence on the collinear PDF is reduced, for $n = 0$ and $n = 1$, due to momentum sum rules fulfilled by each PDF set (though this may be modified by the weak x -dependence of f_{NP} in eqn. (3.15)). The investigation of moments is significant also because ratios for different flavours can be measured independently using lattice methods, see e.g. refs. [48, 85]. It is worth noting that these ratios are scale independent, since the TMD evolution in eqn. (3.10) is multiplicative and x -independent. The ratios of the first moments for the light quarks with respect to the u -quark are shown in fig. 12. One can see that, with respect to point-to-point comparisons, they demonstrate a better global agreement. Similar effects appear for the second and third moments. The corresponding plots are given in the supplementary material.

The extracted values of the CS kernel are shown in fig. 13. In the present ansatz, eqn. (3.11), its NP part is fixed by a single parameter c_0 , whose extracted values are given in tab. 4 and fig. 8. It appears to be dependent on the PDF since the global DY data is not sufficiently accurate to decorrelate non-perturbative behaviors of unpolarized TMDPDFs and the CS-kernel. The inclusion of global SIDIS data should essentially improve this situation, as demonstrated in SV19 [3]. We also observe that the average value of c_0 (among all PDF cases) almost coincides with the one from the SV19 SIDIS+DY extraction: $3.7 \cdot 10^{-2}$ vs. $(3.9 \pm 0.6) \cdot 10^{-2}$. The theory expectation for it is $c_0 \simeq (1.5) \times 10^{-2} \text{GeV}^2$ [45].

Parameter	MSHT20	HERA20	NNPDF31	CT18
λ_1^u	$0.12^{+0.12}_{-0.04}$	$0.11^{+0.07}_{-0.07}$	$0.28^{+0.12}_{-0.10}$	$0.05^{+0.09}_{-0.05}$
λ_2^u	$0.32^{+1.84}_{-0.22}$	$8.15^{+2.09}_{-3.51}$	$2.58^{+1.37}_{-2.05}$	$0.9^{+0.84}_{-0.71}$
λ_1^d	$0.37^{+0.09}_{-0.10}$	$0.44^{+0.09}_{-0.31}$	$0.40^{+0.10}_{-0.22}$	$0.29^{+0.11}_{-0.22}$
λ_2^d	$1.7^{+2.4}_{-1.6}$	$0.11^{+1.14}_{-0.11}$	$1.1^{+2.4}_{-1.0}$	$4.7^{+5.0}_{-4.4}$
$\lambda_1^{\bar{u}} \times 100$	$0.37^{+2.51}_{-0.27}$	$11.6^{+7.1}_{-7.6}$	$8.8^{+10.1}_{-8.6}$	$0.94^{+8.14}_{-0.85}$
$\lambda_2^{\bar{u}}$	$56.^{+6.}_{-12.}$	$6.5^{+5.5}_{-6.4}$	$13.^{+28.}_{-6.}$	$56.^{+4.}_{-22.}$
$\lambda_1^{\bar{d}} \times 100$	$0.12^{+0.18}_{-0.02}$	$35.^{+6.}_{-15.}$	$9.8^{+9.4}_{-9.5}$	$0.12^{+0.86}_{-0.02}$
$\lambda_2^{\bar{d}}$	$1.1^{+2.4}_{-1.0}$	$0.05^{+0.09}_{-0.05}$	$6.1^{+16.7}_{-1.6}$	$0.37^{+2.20}_{-0.26}$
λ_1^s	$0.11^{+0.07}_{-0.10}$	$0.49^{+0.45}_{-0.15}$	$0.25^{+0.15}_{-0.12}$	$0.012^{+0.006}_{-0.011}$
λ_2^s	$5.1^{+3.3}_{-3.4}$	$5.2^{+7.7}_{-5.0}$	$3.0^{+4.3}_{-3.0}$	$9.1^{+4.2}_{-4.5}$
λ_0	$29.^{+53.}_{-10.}$	$339.^{+156.}_{-212.}$	$181.^{+39.}_{-133.}$	$24.^{+73.}_{-11.}$
$c_0 \times 100$	$4.36^{+0.31}_{-0.31}$	$3.27^{+1.23}_{-0.52}$	$2.61^{+0.97}_{-0.61}$	$4.39^{+0.41}_{-0.44}$

Table 4: The values of the NP parameters obtained in the fit.

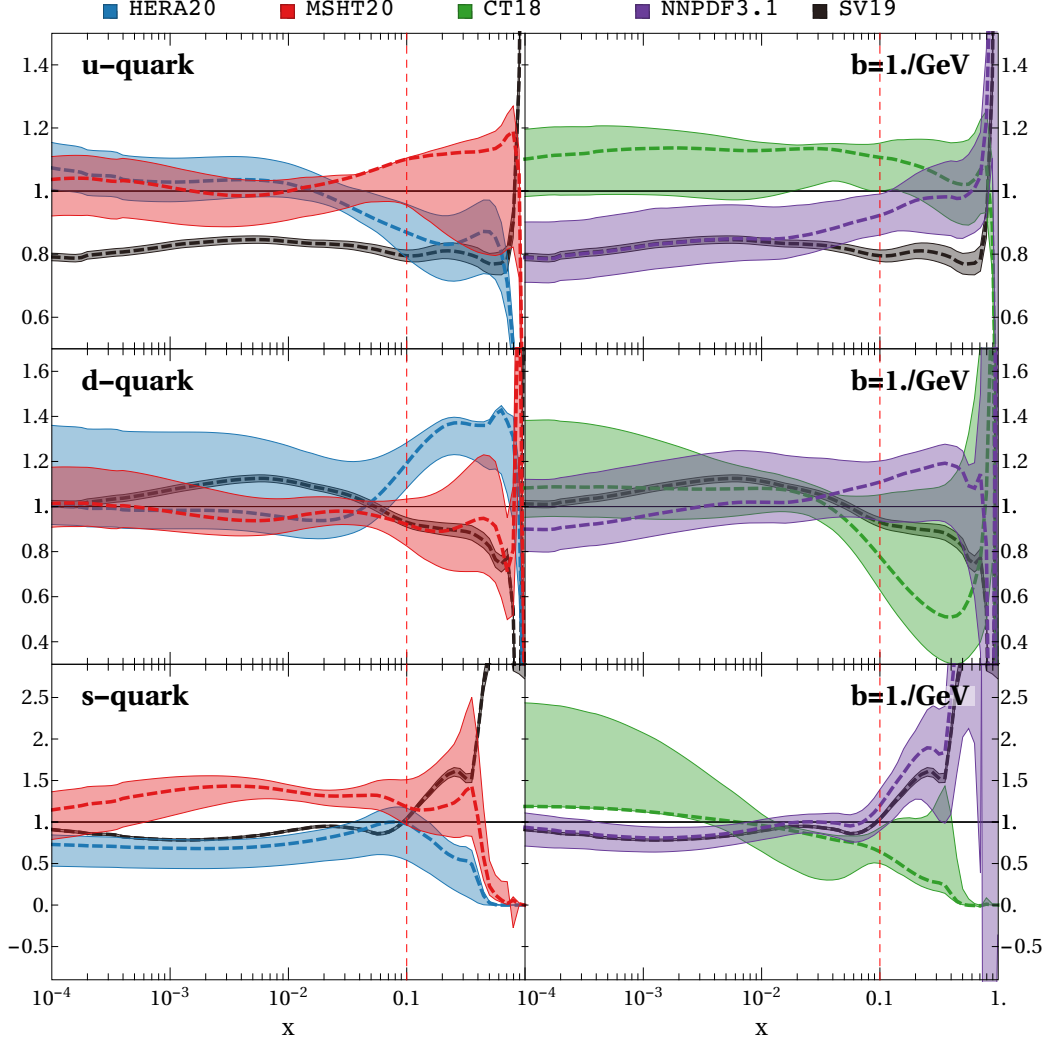


Figure 10: Comparison of uncertainty band for unpolarized TMDPDFs extracted with different PDFs. Here, the slice of optimal TMDPDF at $b = 1\text{GeV}^{-1}$ is shown as the function of x . For convenience of presentation the plot is weighted with the central TMDPDF value averaged between different PDF cases. The red line indicates the position of slice demonstrated in fig.11.

	CDF [86]	D0 [87]	ATLAS [88]			CMS [78]	
			e -channel	μ -channel	combined	e -channel	μ -channel
Points	10	10	2	2	2	4	4
MSHT20	0.66	1.8	2.9	1.6	2.5	8.1	32.
HERA20	0.68	2.0	1.7	0.6	1.2	5.9	23.
NNPDF31	0.70	1.8	2.5	1.3	2.0	7.6	30.
CT18	0.71	1.9	1.7	0.7	1.2	7.1	26.

Table 5: χ^2/N for differential W production using the current extraction of TMD and theoretical errors (including PDF error coming from 1000 replicas).

6.3 Predictions for W -boson production

The flavor dependence of the TMD distributions could significantly impact the description of processes mediated by the W -boson [8, 89, 90]. In this work we have demonstrated that flavor dependence is essential to resolve the PDF bias. Therefore, including W -boson production data in future studies of unpolarized

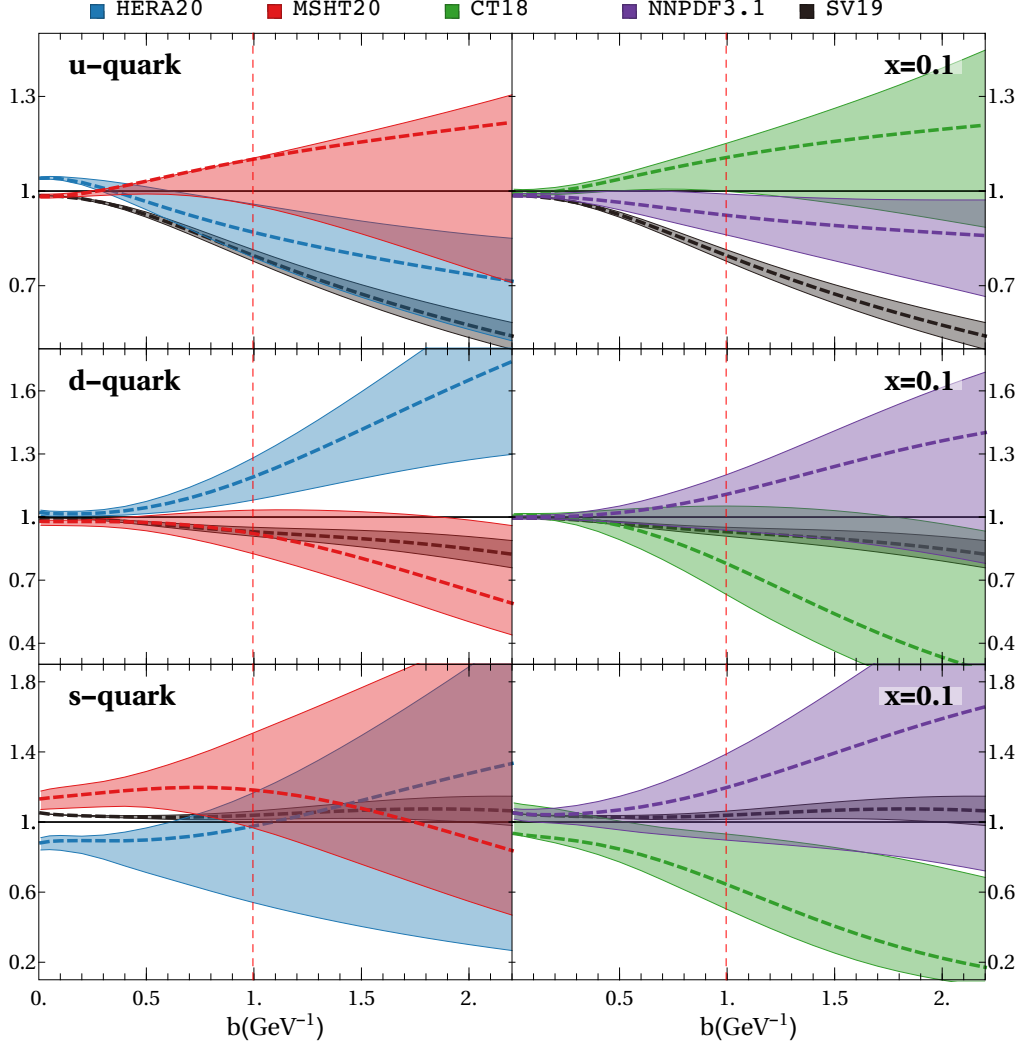


Figure 11: Comparison of the uncertainty band for unpolarized TMDPDFs extracted with different PDFs. Here, the slice of optimal TMDPDF at $x = 0.1$ is shown as a function of b . For convenience of presentation the plot is weighted with the central TMDPDF value averaged between different PDF cases. The red line indicates the position of slice demonstrated in fig. 10.

TMDPDFs is very important.

Since it significantly slows down the fitting procedure, we have not included W -boson production data in this study. Instead, we compare the prediction made with the present extraction to the one made in [37] using the SV19 fit [3]. The computation is performed with the `artemide` code, appropriately adapted for the computation of the transverse-mass-differential cross-section as described in ref. [37]. The values of the χ^2 for comparison with the data by Tevatron and LHC experiments [78, 86–88] are presented in tab. 5. We find a small general improvement compared to the SV19 case [37], which is expected because most of W -boson production data belong to the resummation region.

We briefly comment on the reason why the χ^2 values for the CMS experiment are large in comparison with the other data considered. This measurement is integrated over the full range of the dilepton mass, and the integration range covers low-mass regions in which power corrections in q_T/Q are non-negligible. As a result, the theory prediction deviates from the measurement starting from smaller values of q_T , producing large χ^2 -values. This effect is partially canceled in the cross-section ratios W^-/W^+ and Z/W , which show a substantial agreement between theory and the CMS measurements. Additional plots on this are presented in the supplementary material.

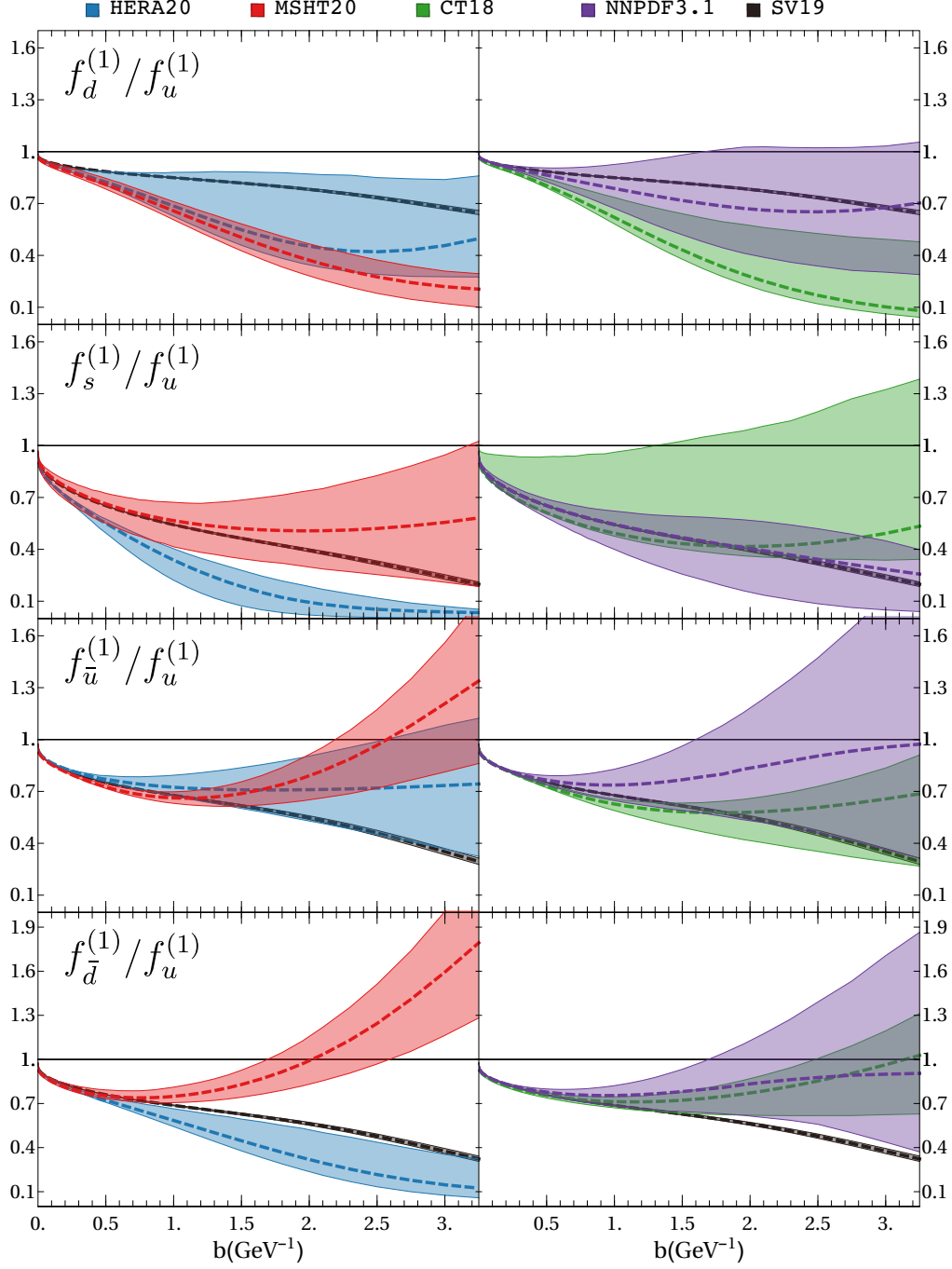


Figure 12: The ratio of the first Mellin moments of unpolarized TMDPDF (6.1) as a function of b for different PDF cases.

7 Conclusions

Collinear PDFs play an important role in the modern phenomenology of TMD distributions, reducing the parametric freedom and establishing the connection with the resummation formalism. The use of PDFs brings a certain degree of intrinsic tensions in the analysis of TMD distributions. These tensions can be revealed by examining anomalies in the shapes of statistical distributions and sensitivity to the PDF sets, which has been found in recent fits of DY and SIDIS experiments [3–6]. We refer to the dependence of extracted TMD distributions on PDFs as PDF bias.

In this paper, for the first time, we address the problem of the PDF bias. We found and demonstrated

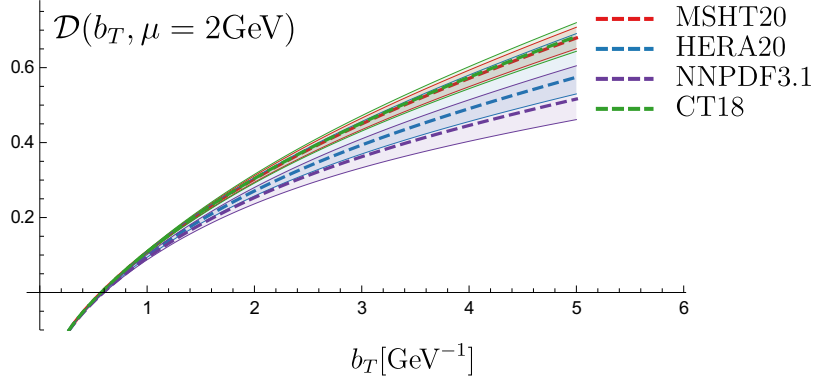


Figure 13: The CS-kernel as a function of b extracted with different PDF inputs.

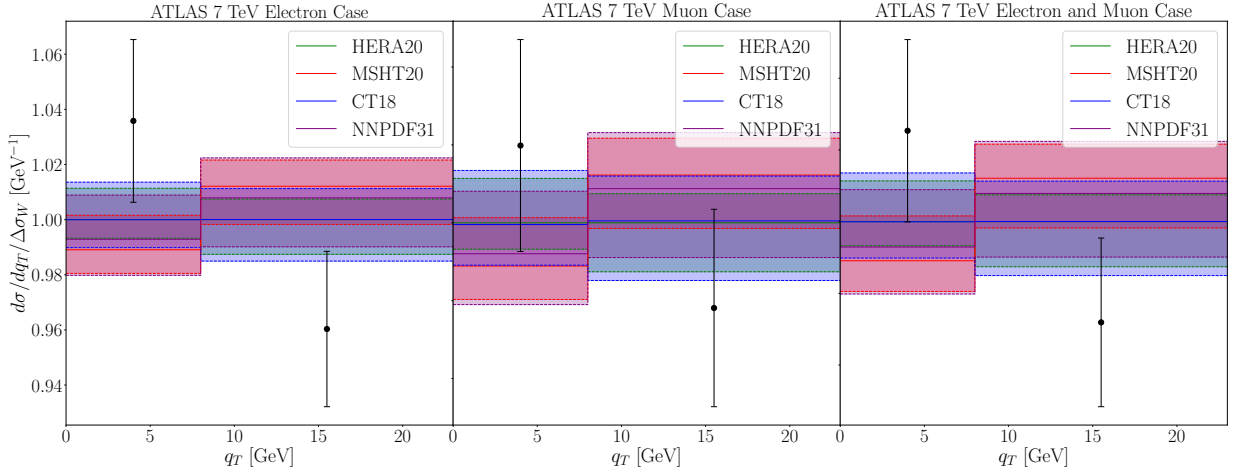


Figure 14: Comparison of the differential cross section for W-boson production measured by ATLAS at 7 TeV with the theory prediction using different PDFs and normalized to HERA20 case.

the following points:

- (i) The PDF bias is substantially reduced once the PDF uncertainties are taken into account.
- (ii) The uncertainties due to PDFs (being propagated to the TMD factorization predictions and to the extracted values of TMDPDF) are larger than those coming from the experimental measurements for all values of b (or p_T).
- (iii) In order to achieve a good fit of DY data and a consistent TMD extraction when using different PDFs sets (we compared HERA20, MSHT20, CT18 and NNPDF3.1), the non-perturbative TMD part must be made flavor dependent. The TMD flavor dependence is expected on theoretical grounds, and the present work shows a first phenomenological evidence.

The ambiguity from PDF has not been considered before, but should be taken into account in the future fits of unpolarized TMD distributions, as an important source of uncertainty. It is also critical for phenomenology of spin-dependent TMD distributions, where the unpolarized cross-section serves as the normalization for the measurements of polarization asymmetries and angular distributions. For example, the uncertainty band of SV19 resulted into 10-15% of the total uncertainty band for the Sivers function [25]. Thus, on one hand, one can expect an extra $\sim 50\%$ uncertainty due to the inclusion of the PDF uncertainty. On the other hand, one can also expect a better agreement between experiments, due to a proper flavor dependence of the unpolarized sector.

At present the TMD flavor effects are entangled with the collinear PDFs. Most likely, additional flavor-sensitive data are needed to shed light on this issue. As an example, we have checked the consistency of our

predictions for the W -boson spectrum. Furthermore, some interesting physical questions (such as the flavor dependence in fragmentation functions and the determination of the W -boson mass) should be addressed together with the problem of the PDF bias. The inclusion of the PDF uncertainty raises the difficulty of the numerical computation, making it very time-consuming. Probably, the method of analysis used here (namely, the separate fits for each replica of PDF distribution) is not optimal, and better methods need to be introduced with the ultimate goal of their joined fit.

Acknowledgments

This study was supported by Deutsche Forschungsgemeinschaft (DFG) through the research Unit FOR 2926, “Next Generation pQCD for Hadron Structure: Preparing for the EIC”, project number 430915485. I.S. is supported by the Spanish Ministry grant PID2019-106080GB-C21. This project has received funding from the European Union Horizon 2020 research and innovation program under grant agreement Num. 824093 (STRONG-2020). S.L.G. is supported by the Austrian Science Fund FWF under the Doctoral Program W1252-N27 Particles and Interactions.

References

- [1] K. Kovařík, P. M. Nadolsky and D. E. Soper, *Hadronic structure in high-energy collisions*, *Rev. Mod. Phys.* **92** (2020) 045003, [1905.06957].
- [2] R. Angeles-Martinez et al., *Transverse Momentum Dependent (TMD) parton distribution functions: status and prospects*, *Acta Phys. Polon.* **B46** (2015) 2501–2534, [1507.05267].
- [3] I. Scimemi and A. Vladimirov, *Non-perturbative structure of semi-inclusive deep-inelastic and Drell-Yan scattering at small transverse momentum*, *JHEP* **06** (2020) 137, [1912.06532].
- [4] V. Bertone, I. Scimemi and A. Vladimirov, *Extraction of unpolarized quark transverse momentum dependent parton distributions from Drell-Yan/Z-boson production*, *JHEP* **06** (2019) 028, [1902.08474].
- [5] I. Scimemi and A. Vladimirov, *Analysis of vector boson production within TMD factorization*, *Eur. Phys. J.* **C78** (2018) 89, [1706.01473].
- [6] A. Bacchetta, V. Bertone, C. Bissolotti, G. Bozzi, F. Delcarro, F. Piacenza et al., *Transverse-momentum-dependent parton distributions up to N^3LL from Drell-Yan data*, *JHEP* **07** (2020) 117, [1912.07550].
- [7] A. Bacchetta, F. Delcarro, C. Pisano, M. Radici and A. Signori, *Extraction of partonic transverse momentum distributions from semi-inclusive deep-inelastic scattering, Drell-Yan and Z-boson production*, *JHEP* **06** (2017) 081, [1703.10157].
- [8] A. Signori, A. Bacchetta, M. Radici and G. Schnell, *Investigations into the flavor dependence of partonic transverse momentum*, *JHEP* **11** (2013) 194, [1309.3507].
- [9] F. Hautmann and H. Jung, *Transverse momentum dependent gluon density from DIS precision data*, *Nucl. Phys. B* **883** (2014) 1–19, [1312.7875].
- [10] P. Kotko, K. Kutak, S. Sapeta, A. M. Stasto and M. Strikman, *Estimating nonlinear effects in forward dijet production in ultra-peripheral heavy ion collisions at the LHC*, *Eur. Phys. J. C* **77** (2017) 353, [1702.03063].
- [11] A. Bermudez Martinez, P. Connor, H. Jung, A. Lelek, R. Žlebčík, F. Hautmann et al., *Collinear and TMD parton densities from fits to precision DIS measurements in the parton branching method*, *Phys. Rev. D* **99** (2019) 074008, [1804.11152].
- [12] N. A. Abdulov et al., *TMDlib2 and TMDplotter: a platform for 3D hadron structure studies*, *Eur. Phys. J. C* **81** (2021) 752, [2103.09741].
- [13] F. Hautmann, H. Jung, M. Kramer, P. J. Mulders, E. R. Nocera, T. C. Rogers et al., *TMDlib and TMDplotter: library and plotting tools for transverse-momentum-dependent parton distributions*, *Eur. Phys. J.* **C74** (2014) 3220, [1408.3015].
- [14] A. Apyan, D. Froidevaux et al., *LHC Electroweak Working Group: W/Z transverse momentum benchmarking*, *CERN* (2021) .

- [15] S. Camarda et al., *DYTurbo: Fast predictions for Drell-Yan processes*, *Eur. Phys. J. C* **80** (2020) 251, [1910.07049].
- [16] F. Coradeschi and T. Cridge, *reSolve — A transverse momentum resummation tool*, *Comput. Phys. Commun.* **238** (2019) 262–294, [1711.02083].
- [17] W. Bizon, X. Chen, A. Gehrmann-De Ridder, T. Gehrmann, N. Glover, A. Huss et al., *Fiducial distributions in Higgs and Drell-Yan production at $N^3LL+NNLO$* , *JHEP* **12** (2018) 132, [1805.05916].
- [18] M. A. Ebert, J. K. L. Michel, I. W. Stewart and F. J. Tackmann, *Drell-Yan q_T resummation of fiducial power corrections at N^3LL* , *JHEP* **04** (2021) 102, [2006.11382].
- [19] T. Becher and T. Neumann, *Fiducial q_T resummation of color-singlet processes at $N^3LL+NNLO$* , *JHEP* **03** (2021) 199, [2009.11437].
- [20] H1, ZEUS collaboration, H. Abramowicz et al., *Combination of measurements of inclusive deep inelastic $e^\pm p$ scattering cross sections and QCD analysis of HERA data*, *Eur. Phys. J.* **C75** (2015) 580, [1506.06042].
- [21] S. Bailey, T. Cridge, L. A. Harland-Lang, A. D. Martin and R. S. Thorne, *Parton distributions from LHC, HERA, Tevatron and fixed target data: MSHT20 PDFs*, *Eur. Phys. J. C* **81** (2021) 341, [2012.04684].
- [22] T.-J. Hou et al., *New CTEQ global analysis of quantum chromodynamics with high-precision data from the LHC*, *Phys. Rev. D* **103** (2021) 014013, [1912.10053].
- [23] NNPDF collaboration, R. D. Ball et al., *Parton distributions from high-precision collider data*, *Eur. Phys. J.* **C77** (2017) 663, [1706.00428].
- [24] A. Vladimirov, *Pion-induced Drell-Yan processes within TMD factorization*, 1907.10356.
- [25] M. Bury, A. Prokudin and A. Vladimirov, *Extraction of the Sivers Function from SIDIS, Drell-Yan, and W^\pm/Z Data at Next-to-Next-to-Next-to Leading Order*, *Phys. Rev. Lett.* **126** (2021) 112002, [2012.05135].
- [26] M. G. Echevarria, Z.-B. Kang and J. Terry, *Global analysis of the Sivers functions at NLO+NNLL in QCD*, *JHEP* **01** (2021) 126, [2009.10710].
- [27] L. A. Harland-Lang, A. D. Martin, P. Motylinski and R. S. Thorne, *Parton distributions in the LHC era: MMHT 2014 PDFs*, *Eur. Phys. J.* **C75** (2015) 204, [1412.3989].
- [28] S. Dulat, T.-J. Hou, J. Gao, M. Guzzi, J. Huston, P. Nadolsky et al., *New parton distribution functions from a global analysis of quantum chromodynamics*, *Phys. Rev.* **D93** (2016) 033006, [1506.07443].
- [29] J. Butterworth et al., *PDF4LHC recommendations for LHC Run II*, *J. Phys.* **G43** (2016) 023001, [1510.03865].
- [30] A. Accardi, L. T. Brady, W. Melnitchouk, J. F. Owens and N. Sato, *Constraints on large- x parton distributions from new weak boson production and deep-inelastic scattering data*, *Phys. Rev. D* **93** (2016) 114017, [1602.03154].
- [31] T. Becher and M. Neubert, *Drell-Yan Production at Small q_T , Transverse Parton Distributions and the Collinear Anomaly*, *Eur. Phys. J.* **C71** (2011) 1665, [1007.4005].
- [32] J. Collins, *Foundations of perturbative QCD*. Cambridge University Press, 2013.
- [33] M. G. Echevarria, A. Idilbi and I. Scimemi, *Factorization Theorem For Drell-Yan At Low q_T And Transverse Momentum Distributions On-The-Light-Cone*, *JHEP* **07** (2012) 002, [1111.4996].
- [34] J.-Y. Chiu, A. Jain, D. Neill and I. Z. Rothstein, *A Formalism for the Systematic Treatment of Rapidity Logarithms in Quantum Field Theory*, *JHEP* **05** (2012) 084, [1202.0814].
- [35] D. Gutierrez-Reyes, I. Scimemi, W. J. Waalewijn and L. Zoppi, *Transverse momentum dependent distributions in e^+e^- and semi-inclusive deep-inelastic scattering using jets*, *JHEP* **10** (2019) 031, [1904.04259].
- [36] F. Hautmann, I. Scimemi and A. Vladimirov, *Non-perturbative contributions to vector-boson transverse momentum spectra in hadronic collisions*, *Phys. Lett. B* **806** (2020) 135478, [2002.12810].
- [37] D. Gutierrez-Reyes, S. Leal-Gomez and I. Scimemi, *W-boson production in TMD factorization*, *Eur. Phys. J. C* **81** (2021) 418, [2011.05351].
- [38] I. Scimemi and A. Vladimirov, *Systematic analysis of double-scale evolution*, *JHEP* **08** (2018) 003, [1803.11089].

- [39] S. M. Aybat and T. C. Rogers, *TMD Parton Distribution and Fragmentation Functions with QCD Evolution*, *Phys. Rev.* **D83** (2011) 114042, [1101.5057].
- [40] M. A. Ebert and F. J. Tackmann, *Resummation of Transverse Momentum Distributions in Distribution Space*, *JHEP* **02** (2017) 110, [1611.08610].
- [41] A. Vladimirov, V. Moos and I. Scimemi, *Transverse momentum dependent operator expansion at next-to-leading power*, 2109.09771.
- [42] M. G. Echevarria, A. Idilbi, A. Schafer and I. Scimemi, *Model-Independent Evolution of Transverse Momentum Dependent Distribution Functions (TMDs) at NNLL*, *Eur. Phys. J.* **C73** (2013) 2636, [1208.1281].
- [43] M. G. Echevarria, I. Scimemi and A. Vladimirov, *Universal transverse momentum dependent soft function at NNLO*, *Phys. Rev.* **D93** (2016) 054004, [1511.05590].
- [44] A. A. Vladimirov, *Soft-/rapidity- anomalous dimensions correspondence*, *Phys. Rev. Lett.* **118** (2017) 062001, [1610.05791].
- [45] A. A. Vladimirov, *Self-contained definition of Collins-Soper kernel*, 2003.02288.
- [46] J. Collins and T. Rogers, *Understanding the large-distance behavior of transverse-momentum-dependent parton densities and the Collins-Soper evolution kernel*, *Phys. Rev.* **D91** (2015) 074020, [1412.3820].
- [47] LATTICE PARTON collaboration, Q.-A. Zhang et al., *Lattice QCD Calculations of Transverse-Momentum-Dependent Soft Function through Large-Momentum Effective Theory*, *Phys. Rev. Lett.* **125** (2020) 192001, [2005.14572].
- [48] M. Schlemmer, A. Vladimirov, C. Zimmermann, M. Engelhardt and A. Schäfer, *Determination of the Collins-Soper Kernel from Lattice QCD*, *JHEP* **08** (2021) 004, [2103.16991].
- [49] P. Shanahan, M. Wagman and Y. Zhao, *Lattice QCD calculation of the Collins-Soper kernel from quasi TMDPDFs*, 2107.11930.
- [50] F. Hautmann, I. Scimemi and A. Vladimirov, *Determination of the rapidity evolution kernel from Drell-Yan data at low transverse momenta*, in *28th International Workshop on Deep Inelastic Scattering and Related Subjects*, 9, 2021. 2109.12051.
- [51] A. V. Konychev and P. M. Nadolsky, *Universality of the Collins-Soper-Sterman nonperturbative function in gauge boson production*, *Phys. Lett. B* **633** (2006) 710–714, [hep-ph/0506225].
- [52] F. Landry, R. Brock, P. M. Nadolsky and C. P. Yuan, *Tevatron Run-1 Z boson data and Collins-Soper-Sterman resummation formalism*, *Phys. Rev.* **D67** (2003) 073016, [hep-ph/0212159].
- [53] F. Landry, R. Brock, G. Ladinsky and C. P. Yuan, *New fits for the nonperturbative parameters in the CSS resummation formalism*, *Phys. Rev.* **D63** (2001) 013004, [hep-ph/9905391].
- [54] F. Hautmann and D. E. Soper, *Parton distribution function for quarks in an s-channel approach*, *Phys. Rev. D* **75** (2007) 074020, [hep-ph/0702077].
- [55] F. Hautmann and D. E. Soper, *Color transparency in deeply inelastic diffraction*, *Phys. Rev. D* **63** (2001) 011501, [hep-ph/0008224].
- [56] F. Hautmann, Z. Kunszt and D. E. Soper, *Hard scattering factorization and light cone Hamiltonian approach to diffractive processes*, *Nucl. Phys. B* **563** (1999) 153–199, [hep-ph/9906284].
- [57] M. G. Echevarria, I. Scimemi and A. Vladimirov, *Unpolarized Transverse Momentum Dependent Parton Distribution and Fragmentation Functions at next-to-next-to-leading order*, *JHEP* **09** (2016) 004, [1604.07869].
- [58] M.-x. Luo, T.-Z. Yang, H. X. Zhu and Y. J. Zhu, *Unpolarized quark and gluon TMD PDFs and FFs at N³LO*, *JHEP* **06** (2021) 115, [2012.03256].
- [59] M.-x. Luo, T.-Z. Yang, H. X. Zhu and Y. J. Zhu, *Quark Transverse Parton Distribution at the Next-to-Next-to-Next-to-Leading Order*, *Phys. Rev. Lett.* **124** (2020) 092001, [1912.05778].
- [60] M. A. Ebert, B. Mistlberger and G. Vita, *Transverse momentum dependent PDFs at N³LO*, *JHEP* **09** (2020) 146, [2006.05329].
- [61] V. Moos and A. Vladimirov, *Calculation of transverse momentum dependent distributions beyond the leading power*, *JHEP* **12** (2020) 145, [2008.01744].

- [62] “**artemide** web-page, <https://teorica.fis.ucm.es/artemide/>
artemide repository, <https://github.com/vladimirovalexey/artemide-public>.”
- [63] A. Buckley, J. Ferrando, S. Lloyd, K. Noerdstrom, B. Page, M. Ruefenacht et al., *LHAPDF6: parton density access in the LHC precision era*, *Eur. Phys. J.* **C75** (2015) 132, [1412.7420].
- [64] H. Dembinski and P. O. et al., *scikit-hep/iminuit*, .
- [65] CMS collaboration, A. M. Sirunyan et al., *Measurements of differential Z boson production cross sections in proton-proton collisions at $\sqrt{s} = 13$ TeV*, *JHEP* **12** (2019) 061, [1909.04133].
- [66] A. S. Ito et al., *Measurement of the Continuum of Dimuons Produced in High-Energy Proton - Nucleus Collisions*, *Phys. Rev.* **D23** (1981) 604–633.
- [67] G. Moreno et al., *Dimuon production in proton - copper collisions at $\sqrt{s} = 38.8$ -GeV*, *Phys. Rev.* **D43** (1991) 2815–2836.
- [68] E772 collaboration, P. L. McGaughey et al., *Cross-sections for the production of high mass muon pairs from 800-GeV proton bombardment of H-2*, *Phys. Rev.* **D50** (1994) 3038–3045.
- [69] PHENIX collaboration, C. Aidala et al., *Measurements of $\mu\mu$ pairs from open heavy flavor and Drell-Yan in $p + p$ collisions at $\sqrt{s} = 200$ GeV*, *Submitted to: Phys. Rev. D* (2018) , [1805.02448].
- [70] CDF collaboration, T. Affolder et al., *The transverse momentum and total cross section of e^+e^- pairs in the Z boson region from $p\bar{p}$ collisions at $\sqrt{s} = 1.8$ TeV*, *Phys. Rev. Lett.* **84** (2000) 845–850, [hep-ex/0001021].
- [71] CDF collaboration, T. Aaltonen et al., *Transverse momentum cross section of e^+e^- pairs in the Z-boson region from $p\bar{p}$ collisions at $\sqrt{s} = 1.96$ TeV*, *Phys. Rev.* **D86** (2012) 052010, [1207.7138].
- [72] D0 collaboration, B. Abbott et al., *Measurement of the inclusive differential cross section for Z bosons as a function of transverse momentum in $p\bar{p}$ collisions at $\sqrt{s} = 1.8$ TeV*, *Phys. Rev.* **D61** (2000) 032004, [hep-ex/9907009].
- [73] D0 collaboration, V. M. Abazov et al., *Measurement of the shape of the boson transverse momentum distribution in $p\bar{p} \rightarrow Z/\gamma^* \rightarrow e^+e^- + X$ events produced at $\sqrt{s}=1.96$ -TeV*, *Phys. Rev. Lett.* **100** (2008) 102002, [0712.0803].
- [74] D0 collaboration, V. M. Abazov et al., *Measurement of the normalized $Z/\gamma^* \rightarrow \mu^+\mu^-$ transverse momentum distribution in $p\bar{p}$ collisions at $\sqrt{s} = 1.96$ TeV*, *Phys. Lett.* **B693** (2010) 522–530, [1006.0618].
- [75] ATLAS collaboration, G. Aad et al., *Measurement of the Z/γ^* boson transverse momentum distribution in pp collisions at $\sqrt{s} = 7$ TeV with the ATLAS detector*, *JHEP* **09** (2014) 145, [1406.3660].
- [76] ATLAS collaboration, G. Aad et al., *Measurement of the transverse momentum and ϕ_η^* distributions of Drell-Yan lepton pairs in proton-proton collisions at $\sqrt{s} = 8$ TeV with the ATLAS detector*, *Eur. Phys. J.* **C76** (2016) 291, [1512.02192].
- [77] CMS collaboration, S. Chatrchyan et al., *Measurement of the Rapidity and Transverse Momentum Distributions of Z Bosons in pp Collisions at $\sqrt{s} = 7$ TeV*, *Phys. Rev.* **D85** (2012) 032002, [1110.4973].
- [78] CMS collaboration, V. Khachatryan et al., *Measurement of the transverse momentum spectra of weak vector bosons produced in proton-proton collisions at $\sqrt{s} = 8$ TeV*, *JHEP* **02** (2017) 096, [1606.05864].
- [79] LHCb collaboration, R. Aaij et al., *Measurement of the forward Z boson production cross-section in pp collisions at $\sqrt{s} = 7$ TeV*, *JHEP* **08** (2015) 039, [1505.07024].
- [80] LHCb collaboration, R. Aaij et al., *Measurement of forward W and Z boson production in pp collisions at $\sqrt{s} = 8$ TeV*, *JHEP* **01** (2016) 155, [1511.08039].
- [81] LHCb collaboration, R. Aaij et al., *Measurement of the forward Z boson production cross-section in pp collisions at $\sqrt{s} = 13$ TeV*, *JHEP* **09** (2016) 136, [1607.06495].
- [82] NNPDF collaboration, R. D. Ball, L. Del Debbio, S. Forte, A. Guffanti, J. I. Latorre, A. Piccione et al., *A Determination of parton distributions with faithful uncertainty estimation*, *Nucl. Phys.* **B809** (2009) 1–63, [0808.1231].
- [83] R. D. Ball et al., *Parton Distribution Benchmarking with LHC Data*, *JHEP* **04** (2013) 125, [1211.5142].
- [84] T.-J. Hou et al., *Reconstruction of Monte Carlo replicas from Hessian parton distributions*, *JHEP* **03** (2017) 099, [1607.06066].

- [85] B. U. Musch, P. Hagler, M. Engelhardt, J. W. Negele and A. Schafer, *Sivers and Boer-Mulders observables from lattice QCD*, *Phys. Rev. D* **85** (2012) 094510, [[1111.4249](#)].
- [86] CDF collaboration, F. Abe et al., *Measurement of the W $P(T)$ distribution in $\bar{p}p$ collisions at $\sqrt{s} = 1.8$ TeV*, *Phys. Rev. Lett.* **66** (1991) 2951–2955.
- [87] D0 collaboration, B. Abbott et al., *Measurement of the shape of the transverse momentum distribution of W bosons produced in $p\bar{p}$ collisions at $\sqrt{s} = 1.8$ TeV*, *Phys. Rev. Lett.* **80** (1998) 5498–5503, [[hep-ex/9803003](#)].
- [88] ATLAS collaboration, G. Aad et al., *Measurement of the Transverse Momentum Distribution of W Bosons in pp Collisions at $\sqrt{s} = 7$ TeV with the ATLAS Detector*, *Phys. Rev. D* **85** (2012) 012005, [[1108.6308](#)].
- [89] A. Bacchetta, G. Bozzi, M. Radici, M. Ritzmann and A. Signori, *Effect of Flavor-Dependent Partonic Transverse Momentum on the Determination of the W Boson Mass in Hadronic Collisions*, *Phys. Lett. B* **788** (2019) 542–545, [[1807.02101](#)].
- [90] A. Signori, *Flavor and Evolution Effects in TMD Phenomenology: Manifestation of Hadron Structure in High-Energy Scattering Processes*. PhD thesis, Vrije U., Amsterdam, 2016.